Late Permian–Early Triassic environmental changes recorded by multi-isotope (Re-Os-N-Hg) data and trace metal distribution from the Hovea-3 section, Western Australia

Svetoslav V. Georgiev[a,*], Holly J. Stein[a, b], Gang Yang[a], Judith L. Hannah[a, b], Michael E. Böttcher[c, d, e], Kliti Grice[f], Alex I. Holman[f], Steven Turgeon[g], Siri Simonsen[b], Christophe Cloquet[h]

[a] *AIRIE Program, Colorado State University, Fort Collins, 80523-1482 CO, USA*

[b] *Institute of Geosciences, University of Oslo, 0316 Oslo, Norway*

[c] *Leibniz Institute for Baltic Sea Research (IOW), Geochemistry & Isotope Biogeochemistry Group, 18119 Warnemünde, Germany*

[d] *Marine Geochemistry, University of Greifswald, 17489 Greifswald, Germany*

[e] *Department of Maritime Systems, Interdisciplinary Faculty, University of Rostock, 18059 Rostock, Germany*

[f] *Western Australian Organic & Isotope Geochemistry Centre, The Institute for Geoscience Research, School of Earth and Planetary Sciences, Curtin University, Perth, WA, Australia*

[g] *Microbiogeochemistry, Carl-von-Ossietzky University, 26111 Oldenburg, Germany*

[h] *CNRS, UL-UMR7358, 15 rue Notre Dame des Pauvres, 54500, Vandoeuvre-lès-Nancy, France*

Abstract

The temporal coincidence between the Late Permian mass extinction (LPME) and the emplacement of Siberian Traps basalts suggests a causal link between the two events. Here, we discuss stratigraphic changes of organic and inorganic (including isotopic) geochemical properties of marine sediments across the Permian–Triassic boundary (PTB) in the Hovea-3 core, Western Australia, a key PTB section in the southern Neo-Tethys ocean. These data are compared with published data from the Meishan section, southern China, and from the Opal

Creek section in western Canada, providing a view of Tethys and Panthalassa changes at the PTB. Trace metal and N-isotopic data, together with organic matter properties suggest that anoxic conditions were established prior to the LPME, intensified close to the LPME, and continued with photic-zone euxinia into the Early Triassic. For the Hovea-3 section, Re-Os ages confirm Changhsingian (253.5 ± 1.4 Ma) deposition of the dated interval sampled immediately below the stratigraphic level characterized by major lithological and isotopic changes. Evaluation of Re-Os, N, and Hg elemental and isotopic data for Hovea-3 suggests that anoxic conditions in the latest Permian were generally unrelated to direct magmatic contributions. A major increase in the initial Os isotopic ratio of Lower Triassic shales suggest an ~8x increase in the Early Triassic continental runoff, based on moderately conservative assumptions for end-members contributing Os to the P−Tr ocean. Comparison to other PTB sections confirms a global signal of increasing Re/Os ratios in the Late Permian, and major and long-lived changes in the isotopic composition of the post-extinction ocean. A distinct peak in Hg concentrations carrying a volcanic isotopic signature, also identified in other PTB sections, likely represents a major pulse of Siberian Trap volcanism. This Hg peak in the Hovea-3 section, however, is detected above the stratigraphic level containing multiple other widely recognized and more permanent geochemical changes. Therefore, direct volcanic inputs to the Permian–Triassic Ocean likely post-dates the LPME in this Western Australian section.

1. Introduction

The Late Permian mass extinction (LPME) is the greatest reduction of biodiversity known in Earth's history. The LPME proceeded rapidly at ~251.9 Ma (Burgess et al., 2014) and coincided with significant climate warming and profound changes in oceanic and atmospheric chemistry (e.g. Knoll et al., 2007; Payne and Clapham, 2012; Sun et al., 2012; Shen et al., 2013). These changes were likely caused by complex feedbacks related to massive volatile release during the eruption of the Siberian Traps, one of the largest flood basalt provinces, and associated shallow magmatic intrusions into carbon-rich sediments (e.g., Erwin, 1994; Svensen et al., 2009; Payne and Clapham, 2012; Burgess et al., 2014). The LPME sparks significant scientific interest both in

58   terms of permanently altering the evolutionary course of our planet, and in providing an analog

59   for present day warming trends. The current understanding of the causes, effect, and timing of

60   the LPME comes from a very large and growing number of diverse studies on multiple Permian–

61   Triassic boundary (PTB) sections worldwide. Importantly, comparisons between different

62   sections establish global patterns of extinction, related geochemical changes, the sequence of

63   events, and the main causes for the LPME. Bond and Wignall (2010), for example, outline a

64   distinct paleolatitude zonation with the most severe and persistent anoxia developing in higher

65   paleolatitudes (Australia and Greenland), whereas equatorial settings record shorter and

66   somewhat less severe anoxia.

67   However, the geographic distribution of studied PTB marine sections is uneven (e.g., see

68   Algeo and Twitchett, 2010; Bond and Wignall, 2010; Shen et al., 2019). Best represented are

69   sub-equatorial locations mostly in the western (e.g., Italy, Austria, Hungary, Slovenia) and

70   eastern (e.g., China, Vietnam) Paleotethys Ocean and remnants of the Panthalassa oceanic floor

71   preserved in present-day Japan. Mid- to high-latitude locations are more densely sampled in the

72   northern hemisphere (e.g., Greenland, Spitzbergen, Canada, Canadian Arctic), whereas only few

73   marine PTB sections have been studied from mid- to high-latitudes in the southern hemisphere

74   Neotethys Ocean (Kashmir, Australia). More geochemical data from high-latitude Neotethys

75   localities are needed to correlate distant sections, to establish global patterns in geochemical

76   changes associated with the LPME, and ultimately to better understand the processes operating

77   across the PTB transition.

78   Here, we present a diverse set of organic and inorganic geochemical parameters for

79   sediments deposited in a high-latitude Neotethys locality. The Hovea-3 section in Western

80   Australia has previously been characterized in terms of sedimentology, biostratigraphy, amount

81   and type of organic matter (OM), δ^{13}C of bulk OM, of organic extracts, and of specific organic

82   compounds, δD of kerogen and δ^{34}S of pyrite and bulk rocks, biomarker contents and pyrite

83   morphology (e.g., Thomas et al., 2004; Thomas and Barber, 2004; Grice et al., 2005a; Grice et

84   al., 2005b, Nabbefeld et al., 2010a; Nabbefeld et al., 2010b, Bond and Wignall, 2010; Grotheer

85   et al., 2017). These studies highlight some unique aspects of the Hovea-3 section compared with

86   other PTB sections worldwide. The high paleolatitude of this section provides the southernmost

87   available sedimentary record in the marine environment during the Late Permian. Being the most

88   distant record from the presumed cause of the LPME, the Siberian Traps, geochemical changes

89 in the Hovea-3 core can be used to evaluate global changes near the PTB (e.g., Bond and

90 Wignall, 2010; Nabbefeld et al., 2010a). Unlike all other reported PTB sections, the Hovea-3

91 section entirely comprises organic-rich (generally 1–4 wt% TOC, total organic carbon)

92 lithologies (Thomas et al., 2004). This organic richness allows better characterization and

93 quantification of the sources of organic matter and provides a major sink for key geochemical

94 tracers. In addition, the Hovea-3 section comprises similar lithologies dominated by siltstone-

95 shale, thereby aiding more straightforward distinction of geochemical parameters affected by

96 lithological, as opposed to environmental changes. Finally, many PTB sections regardless of

97 their location contain organic-rich uppermost Permian sediments with abundant marine OM,

98 whereas globally most of the lowermost Triassic sediments, even those that are more organic-

99 rich, largely contain more refractory, terrestrially derived OM (see discussion and references in

100 Georgiev et al., 2015a). In strong contrast, the Hovea-3 section shows the reverse relationship

101 with terrestrially-dominated OM in the Permian, and abundant marine-derived OM in the

102 Triassic portion of the section (Thomas et al., 2004). Because of this, the lowermost Triassic in

103 Hovea-3 is considered an excellent quality source rock that likely produced most of the

104 hydrocarbon accumulations in the northern Perth Basin (Thomas and Barber, 2004; Gorter et al.,

105 2009). From a geochemical point of view, it is important that the geochemistry of the Triassic

106 sediments in the Hovea-3 section is essentially unaffected by terrestrial OM contributions and,

107 therefore, reflects the changing marine biogeochemistry after the LPME.

108   Despite the number of studies focusing on the Hovea-3 PTB section (e.g., Thomas et al.,

109 2004; Thomas and Barber, 2004; Grice et al., 2005a; Grice et al., 2005b, Nabbefeld et al., 2010a;

110 Nabbefeld et al., 2010b, Bond and Wignall, 2010), a quantitative geochemical characterization of

111 the major and trace element contents of the sediments is needed to provide a solid background

112 for correct interpretation of geochemical data. In addition, available biostratigraphic constraints

113 for the age of the sediments are relatively sparse, rely on regional and broader correlations, and

114 are not backed up by radiometric ages. The existing geochemical records for the Hovea-3 core

115 show a sharp change in $\delta^{13}C_{org}$ and the type of organic matter (e.g., Thomas et al., 2004)

116 suggesting a depositional hiatus near the PTB (Grice et al., 2005b; Gorter et al., 2009). However,

117 fairly uniform $\delta^{13}C_{org}$ within the Permian, and within the Triassic portions cannot be used for

118 refined regional or global correlations. Instead, stratigraphic changes in Hg contents or the

119 isotopic composition of Hg or Os may be used for global correlations. Hg data in particular have

120 been reported for many PTB sections, providing a solid base for global comparisons (e.g.,

121 Grasby et al., 2017; Shen et al., 2019a; Wang et al., 2019). These include recently reported Hg

122 concentrations and limited Hg-isotopic data for the Hovea-3 section (Sial et al., 2020).

123   To address these concerns, we present results from an extensive geochemical (major and

124 trace elements, N, Hg and Os isotopes) and Re-Os geochronology study on Permian and Triassic

125 sediments from the Hovea-3 core with the following aims:

126   1) To provide direct radiometric age constraints for the Hovea-3 sediments.

127   2) To reconstruct redox conditions during sediment deposition.

128   3) To trace stratigraphic variations in key organic and inorganic parameters and stable

129   isotope ratios and use these to identify regional processes operating during the PTB

130   transition in Western Australia.

131   4) To compare geochemical variations in the Hovea-3 sections with other PTB localities and

132   discuss changes in global ocean chemistry during the PTB transition, including the

133   relative timing of significant events related to the LPME.

134

135 **2. Geological background**

136

137   The northern Perth Basin, onshore Western Australia, is a ~750 km long and ~80 km wide

138 north-south elongate basin centered ~140 km north of the city of Perth (Fig. 1a). Multiple

139 episodes of rifting, subsidence, uplift and erosion contribute to its complex geologic history (e.g.,

140 Cooper et al., 2015). During the Late Permian, the basin was situated on the Perigondwanan

141 margin at mid- to high-paleolatitudes of ~60 °S, facing the southern Neotethys ocean (Fig. 1b).

142 The Hovea-3 borehole was drilled in 2002 in the northern parts of the basin (29°19′9.17″S,

143 115°2′23.29″E) by Origin Energy and partner Arc Energy as an appraisal well. The Hovea-3 core

144 records a major marine flooding event in the Late Permian, marked by deposition of PTB

145 (Changhsingian-Induan) shallow marine shelf sediments of the Kockatea Formation (Fm) on top

146 of coarse-grained foreshore-shoreface sandstones of the Upper Permian (Capitanian-

147 Wuchiapingian) Dongara Fm (Fig. 1c; Thomas and Barber, 2004; Gorter et al., 2009). The

148 overlying Olenekian-Anisian Woodada Fm not shown on Fig. 1c comprises mostly deltaic

149 claystone and siltstone (Thomas et al., 2004; Gorter et al., 2009).

150   This study focuses on lithologies from the lower part of the Kockatea Fm that straddle the

151   PTB. A ~28-m-thick interval, called the Hovea Member (Mb), comprises sediments relatively

152   rich in OM (about 1-4 wt% TOC) that contain characteristic marine fossils of Changhsingian

153   (latest Permian) and Griesbachian (earliest Triassic) age (Fig. 1c; Thomas et al., 2004). The

154   Hovea Mb is further subdivided into two main intervals based mostly on the type of organic

155   matter present in the sediments: a lower Inertinitic Interval and upper Sapropelic Interval

156   (Thomas et al., 2004); these are abbreviated here as INI and SPI, respectively.

157   The INI consists of ~11.5-m-thick and variably bioturbated fossiliferous black mudstone,

158   sandy siltstone, and shelly storm beds, deposited in a shallow marine setting during the early

159   stages of a Late Permian marine transgression (Thomas et al., 2004). OM here is mostly (50-

160   70%) opaque charcoal and wood fragments of continental origin, with rare spores and pollen,

161   and 13-30% amorphous OM with small amounts of spinose acritarchs. Rock-Eval hydrogen

162   indices for this interval are invariably low, below 100 (Thomas et al., 2004; Gorter et al., 2009;

163   this study).

164   The overlying SPI consists of ~14.5-m-thick alternation of dark, finely laminated mudstone

165   and thin limestone with pervasive syn-sedimentary carbonate cement. This part of the sequence

166   was deposited below wave base, but within the photic zone, as indicated by the presence of algal

167   mats and small stromatolite communities near the top of the Hovea Mb (Thomas et al., 2004).

168   OM in the Sapropelic Interval is abundant (up to 4 wt% TOC), and with high Rock-Eval

169   hydrogen indices between 400 and 800

170   mg hydrocarbons/g TOC, which combined indicate good oil-generation properties. Most of the

171   organic content (50-75%) is yellow-brown amorphous OM of probable marine origin, which

172   sometimes forms sheets of 'algal laminites' (Thomas et al., 2004). The additional 20-40% is

173   structured OM dominated by a restricted assemblage of spinose acritarchs (*Micrhystridium* and

174   *Veryhachium* spp.). Spores, pollen and other continental material are rare (Thomas et al., 2004).

175   The top of the Hovea Mb is marked by a regionally extensive 2-m-thick limestone bed known as

176   the limestone marker (Fig. 1c; Thomas and Barber, 2004).

177

178   **3. METHODS**

179

180   **3.1. Sample preparation**

181   Four sets of samples from the Hovea-3 drill core accessed at different times were analyzed in

182   this study; these sets are clearly identified in the Supplementary Material. For set #1, about 1-

183   cm-thick shale intervals were manually separated along core lamination or cut with a diamond

184   blade precision saw, dried at room temperature if necessary, and powdered in an agate ball mill

185   or in a corundum mortar and pestle using established protocols (Georgiev et al., 2017). Separate

186   powder splits were used for Re-Os, trace elements, Rock-Eval, total organic carbon (TOC),

187   mercury (Hg) and nitrogen contents and stable isotopes, and biomarker analyses. Sample set #2

188   was similarly prepared in Curtin University and analyzed for selected trace metals. Sample sets 3

189   and 4 constitute aliquots of shale powders discussed in Grice et al. (2005a) and Nabbefeld et al.

190   (2010a), respectively). These were analyzed here for new types of geochemical information

191   (major and trace metals, and TOC, N, and Hg contents) that were not previously reported for

192   these samples.

3.2. Re-Os analyses

194   Shale powders from set #1 were digested, chemically treated, and measured using established

195   protocols for Re–Os analyses at the AIRIE Program (Georgiev et al., 2017). Pre-weighed

196   powders (0.15–0.58 g) were combined with known amounts of ^{185}Re and ^{190}Os isotopic tracers

197   and 10–12 mL of CrO_3-H_2SO_4 acid in Carius tubes; sealed tubes in metal jackets were heated at

198   240 °C for 24 h. Osmium was isolated from the digested solutions by liquid-liquid extraction

199   into chloroform and then into HBr (Cohen and Waters, 1996), and purified by two

200   microdistillation steps using HBr and CrO_3-H_2SO_4 (Birck et al., 1997). After reduction of excess

201   Cr^{6+} in the remaining solutions to Cr^{3+} using SO_2, rhenium was isolated and subsequently

202   purified using anion exchange column chemistry (details in Georgiev et al., 2018). Rhenium and

203   Os were loaded on separate outgassed Pt filaments and measured as ReO_4^- and OsO_3^- species,

204   respectively, on Thermo-Fisher Triton and Triton Plus thermal ionization mass spectrometers at

205   AIRIE Program. ^{185}Re and ^{187}Re intensities were simultaneously measured on Faraday cups with

206   10^{11} ohm amplifiers at 4–6 filament temperatures (between ~750 °C and ~840 °C); the mean

207   value and the standard deviation of these measurements were used for further data reduction.

208   Osmium isotopic ratios were measured as 50 individual scans on an axial electron multiplier in

209   peak-jumping mode at a filament temperature of ~730 °C. The mean Os isotopic ratios with their

210   associated standard error of the mean were used for further data reduction.

211   Samples were analyzed in 11 analytical batches that each comprised 8–10 samples and a total

212   analytical blank (TAB) to record Re-Os contributions from digestion, chemical, and mass-

213   spectrometry procedures. Measured TAB were 0.22 ± 0.13 pg Os, with $^{187}Os/^{188}Os = 0.24 ± 0.11$

214   (1 SD, n = 11). Rhenium blanks were more variable, as the Re content of the CrO_3 reagent used

215   for sample digestion varied with different purchased batches. Therefore, TAB for Re are

216   summarized as three groups with Re = 11.7 ± 1.2 (n = 4), 48.6 ± 6.1 (n = 6), and 99.8 (n = 1) pg

217   Re, respectively. Re and Os blanks represent on average 1.7% Re and 0.5% Os of the total (blank

218   + sample) Re and Os measured during shale analyses; blank contributions for individual samples

219   are given in the Supplementary Material. Although the blank contributions for Re are somewhat

220   elevated, these contributions were stable over long periods of time and over multiple batches of

221   samples (until the purchase of new CrO_3). Therefore, the blank correction applied to our samples

222   is accurate, even when Re blank contributions are somewhat elevated.

223   Re (1407 molybdenite processed through column chemistry) and Os (N-4 in-house solution)

224   standards were repeatedly analyzed with each sample batch, yielding $^{185}Re/^{187}Re = 0.59705 ±$

225   0.00036 (1 SD, n = 12) and $^{187}Os/^{188}Os = 0.1239 ± 0.0006$ (1 SD, n = 13), respectively. These

226   values agree with the range of natural $^{185}Re/^{187}Re = 0.59738 ± 0.00039$ (95% confidence limit;

227   Gramlich et al., 1973) and with the long-term measurements of the N-4 standard at AIRIE

228   Program ($^{187}Os/^{188}Os = 0.1237 ± 0.0007$, 1 SD, n = 261).

229   Measured Re and Os isotopic data were corrected for contributions from the isotopic tracer,

230   analytical blanks, heavy oxygen isotope contribution (Nier, 1950) and mass fractionation (for Os,

231   using $^{192}Os/^{188}Os = 3.082707$). Propagated uncertainties include uncertainties from counting

232   statistics, weighing, spike and blank contributions and their isotopic ratios, and an error

233   magnification based on spike-sample ratios. Re–Os isochron regression statistics and plots were

234   made using the Isoplot 4.15 Excel add-in (Ludwig, 2003). Discussion of osmium contents is

235   based the ^{192}Os isotope, which is stable, non-radiogenic (age-independent), and the most

236   abundant Os isotope. Initial $^{187}Os/^{188}Os$ ratios are calculated from measured present-day

237      $^{187}Os/^{188}Os$ and $^{187}Re/^{188}Os$ ratios by accounting for the ingrowth of ^{187}Os through radioactive

238   decay of ^{187}Re with time (251.9 Ma or as noted in the text or figure captions).

239

240   **3.3. Total organic carbon and Rock-Eval data**

241   TOC and Rock-Eval data for set #1 were obtained at Geomark Rock Source (USA). Limiting

242   repeatability is 10% for TOC data and 10–20% for the Rock-Eval peaks (see additional details in

243   Georgiev et al., 2015a). The Rock-Eval parameters describe the quality of OMin organic-rich

244   sedimentary rocks (Peters, 1986). Four parameters are recorded during progressive heating of

245   rock powders (Rock-Eval pyrolysis). These are the free hydrocarbons released at lower

246   temperatures (S1 peak; mg/g rock), the hydrocarbons produced through thermal cracking of

247   kerogens at higher temperatures (S2 peak; mg/g rock), the amount of CO_2 released (S3 peak;

248   mg/g rock), and the temperature of maximum hydrocarbon production (T_{max}). Important

249   derivative parameters include the hydrogen index (HI = S2/TOC mg/g TOC; a proxy for the

250   hydrogen content of kerogens), the oxygen index (OI = S3/TOC, mg/g TOC; a proxy for the

251   oxygen content of kerogen), S1/TOC ratio (a measure of oil presence), and the production index

252   (PI, S1/[S1+S2]; a measure of thermal maturity and/or oil staining). Samples from set #3 were

253   analyzed for total sulfur and total and inorganic carbon at the Institute for Chemistry and Biology

254   of the Marine Environment, University of Oldenburg (ICBM) as described by Turgeon &

255   Brumsack (2006).

256   **3.4. Inorganic major and trace elements**

257   Trace metal contents for shales from set #1 were obtained from Actlabs (Canada) using their

258   standard multi-acid (near) total digestion. The limiting repeatability of these measurements is

259   generally better than 10% (see additional details in Georgiev et al., 2015a). Selected trace

260   element contents were analyzed in samples from set #2 at Curtin University by ICP-MS.

261   Samples from set #3 were analyzed for inorganic major and trace elements at ICBM

262   following methods described by Turgeon & Brumsack (2006). Further, samples from set #4 were

263   analyzed at Leibniz IOW after acid-digestion using ICP-OES following the methods described

264   by Kowalski et al. (2012) and Wegwerth et al. (2016).

265   **3.5. Mercury and nitrogen**

266   The $^{15}N/^{14}N$ isotopic ratio (total nitrogen) is reported for selected samples from set #1 using

267   the standard delta (δ) notation for per mil (‰) difference between the isotope ratio in the sample

268   and air. The δ-values are equivalent to mU (milli Urey; Brand & Coplen, 2012). Samples were

269   measured using a Europa Scientific 20-20 isotope ratio mass spectrometer linked to a Europa

270   Scientific RoboPrep-CN elemental analyzer at Iso-Analytical (UK) (see additional details in

271   Georgiev et al., 2015a).

272   Mercury (Hg) concentrations in samples from set #1 (0.04–0.27 g aliquots) were analyzed

273 using a DMA-80 Evo direct mercury analyzer (Milestone Srl, Italy) at the AIRIE Program.

274 Quality was monitored through multiple analyses of two standards that were repeatedly

275 measured in-between samples. Hg contents of the NIST SRM 1632e bituminous coal measured

276 at AIRIE Program are 136.8 ± 10.7 ppb (n = 28, all uncertainties are 2 SD), which matches the

277 certified value of 135.1 ± 3.5 ppb Hg. Similarly, measured Hg contents for the USGS SDO-1

278 shale of 206.2 ± 9.2 ppb (n = 15) match reported values of 210 ± 2.6 ppb (Marie et al., 2015) and

279 213.4 ± 29.8 ppb (Zheng et al., 2018) for this material. Analyses of multiple powder aliquots

280 (0.04–0.26 g) of a single Hovea-3 shale from 1976.4900-1976.4815 m depth yielded 73.7 ± 3.2

281 ppb Hg (n = 11).

282   Samples from set #3 were analyzed with a DMA-80 analyzer at IOW with a detection limit

283 of about 0.15 µg/kg, as described by Leipe et al. (2013). Signal calibration was carried out with

284 the CRM (BCR) 142R CRM and the SRM 2709 soil standard. Relative standard deviations for

285 measured reference materials (ABSS-1, MBSS-1, BCR 142R) yielded relative deviations below

286 5% from the mean value (Leipe et al., 2013).

287   Stable isotopes (198, 199, 200, 201, 202) of Hg were analyzed simultaneously in 30 samples

288 from set #1 using a Thermo Neptune+ MC-ICP-MS. Samples were introduced through cold

289 vapor generation using Hydride generator CETAC HGX-200 and $SnCl_2$ to reduce Hg; more

290 details can be found in Estrade et al. (2010) and Meier et al. (2016). Multiple analyses of the

291 commonly accepted NIST 3133 reference material bracketed the sample runs Results are

292 reported using mass ^{198}Hg as a reference for the δ and using δ^{202}Hg to calculate Δ^{199}Hg and

293 Δ^{201}Hg. Descriptions of the equations can be found elsewhere (Estrade et al., 2010, Blum et al.,

294 2014).

295   Two standard solutions (F65 A and RL24H) were used to check the instrument accuracy and

296 reproducibility and results given in the Supplementary Data Table are similar to the reported

297 ones (Estrade et al. 2009) within uncertainties. In addition, an international reference material,

298 SDO-1 was introduced along with the sample series to control accuracy and reproducibility;

299 uncertainties on the mean SDO-1 values (n=6) are used as representative for sample analyses.

300 Our SDO-1 results, shown in the Supplementary Data Table, are equivalent within uncertainties

301 with SDO-values reported by Zheng et al. (2018), except for slightly more negative δ^{202}Hg

302 (−0.55‰ in this study; −0.38‰ in Zheng et al., 2018). This 0.17‰ difference in δ^{202}Hg between

303 the two studies is similar to their combined uncertainties (~0.10‰), may partly reflect some

304 sample heterogeneity, and is substantially smaller than δ^{202}Hg variations of ~2‰ recorded in

305 Hovea-3 shales. Uncertainties for Δ^{199}Hg and Δ^{201}Hg are 0.08‰ and 0.06‰, respectively.

3.6. Biomarkers

307 Relative abundances of C_{33} n-alkylcyclohexane (C_{33} n-ACH) and the regular n-C_{34} alkane

308 were measured for 73 shale samples from set #1 by GC-MS. Powdered shale (2-4 g) was

309 extracted ($\times$3) in an ultrasonic bath with a mixture of 9:1 dichloromethane / methanol. Extracts

310 were shaken overnight with activated copper to remove elemental sulfur, and separated into

311 saturate, aromatic and polar fractions (see Grice et al., 2005a). Saturate fractions were analyzed

312 using a HP 6890 gas chromatograph coupled to a 5973 mass-selective detector (method as per

313 Holman et al., 2014).

3.7. SEM imaging

315 Representative fingernail-sized shale sheets from five intervals in the Hovea-3 core from

316 set #1 were sampled to evaluate particulate matter and textural and mineralogical changes

317 spanning the latest Permian to the earliest Triassic. The SEM data were acquired on a Hitachi

318 SU5000 FE-SEM (Schottky FEG) using energy-dispersive X-ray spectroscopy (EDS; Dual

319 Bruker Quantax SFlash 30 EDS system). Images were taken both in SE mode (secondary

320 electrons) and BSE mode (back scatter electrons). A semi-quantitative chemical analysis is

321 provided by EDS.

322

4. Results

324

325 Stratigraphic variations of selected geochemical parameters (Figs 2 and 3) are briefly

326 summarized below and addressed in more detail in the relevant discussion sections. Full

327 analytical results are given in the Supplementary Material (SM), which also contains supporting

328 geochemical plots and SEM images.

329 According to Thomas et al. (2004), the boundary between the inertinitic (INI) and sapropelic

330 intervals (SPI) marks the PTB in the Hovea-3 section. Representative SEM images for the INI

331 (Permian) show an illite-dominated matrix with abundant OM, predominantly framboidal but

332 some octahedral or dodecahedral pyrite, chlorite, barite, tabular gypsum crystals, minor celestite,

333 detrital monazite, biotite, and sparse rutile (Fig. S1). The SPI is characterized by calcite matrix

334 with kaolinite and illite, more abundant OM, pyrite (framboidal and some octahedral) and
335 marcasite, lack of gypsum, and more abundant celestite (Fig. S2). This boundary between the
336 two intervals is characterized by notable changes in the major and trace element content of
337 studied samples. For example, Al contents, a measure for the detrital input to sediments, rapidly
338 decrease from 6–8 wt% in Permian shales down to about 2–4 wt% above the boundary and then
339 rebound to higher values of 8–10 wt% up-section (Fig. 2a). Sulfur contents increase from 1–2
340 wt% in the Permian strata to almost 6 wt% in the lowermost SPI, and remain generally high (2–5
341 wt%) in the Triassic (Fig. 2b); Fe contents closely mirror this S trend (Fig. S3). Calcium and
342 carbonate contents have low values in the Permian INI, sharply increase above the contact with
343 the SPI and then decrease to low values up-section (Fig. 2m; Fig. S3); Mn concentrations
344 generally correlate well with carbonate contents (Fig. S3). The concentration of redox-sensitive
345 trace metals like Mo and U (Fig 2c, d), and redox-indicative ratios like S/TOC and Fe/Al (Fig 2f,
346 g) generally have lower values in the INI, a clear peak near the Inertinitic-Sapropelic boundary,
347 and overall higher values up-section.

348 The amount of organic carbon (Fig. 2h) is generally lower (~1–3 wt%) in the INI than in the
349 SPI (~2–4 wt%). TOC contents decrease from 1992 m to 1984 m depth, generally increase from
350 there to 1975 m depth, and again decrease towards the top of the SPI at 1969 m depth (Fig. 2h).
351 Rock-Eval parameters and particularly the hydrogen index (HI), a measure for the type of OM,
352 reveal major differences between the two studied intervals. Low HI of 23–42 mg hydrocarbons/g
353 TOC in the II and high HI of ~300–800 mg hydrocarbons/g TOC in the Sapropelic Interval (Fig.
354 2j) mark a major shift in the type of OM preserved in the Hovea-3 section (Thomas et al., 2004;
355 Fig. 2i). Noticeable differences between the two intervals are also visible in the T_{max} parameter, a
356 measure for the thermal maturity of the OM (Fig 2k), and in the S1/TOC parameter, a measure
357 for the amount of free hydrocarbons per unit OM (Fig. 2l). Our biomarker data (Fig. 2n) further
358 delineate and confirm the major shift to higher $C_{33}n$-ACH/n-C_{34} ratios in the SPI reported by
359 Grice et al. (2005b).

360 The major shift in the amount, type, and Rock-Eval properties of OM between the INI and
361 SPIs also coincides with major negative shifts in $\delta^{13}C$ and δD of bulk kerogens and extracted
362 hydrocarbons (Fig. 3a; Thomas et al., 2004; Grice et al., 2005a; see also Nabbefeld et al., 2010a).
363 In contrast, $\delta^{34}S_{pyrite}$ gradually increases up-section from ~−50‰, and after a modest dip to more
364 negative values at the PTB stabilizes at about −27‰ in the SPI (Fig. 3b; Grice et al., 2005a;

365   Nabbefeld et al., 2010a). Re contents and ^{187}Re/^{188}Os ratios are low in the basal INI, increase

366   significantly from 1984 m to the PTB where they reach the highest values, and then fall back to

367   low levels throughout the SPI (Fig. 3h, j), in a pattern somewhat resembling the stratigraphic

368   profile for U (Fig. 2d). Osmium contents are generally higher in the INI, with a maximum at

369   1983 m depth (Fig. 3i). Initial ^{187}Os/^{188}Os ratios (Os$_i$; Fig. 3k) are consistently lower in the INI

370   (0.68 ± 0.15 1SD, n = 61, one sample excluded) than in the SPI (1.46 ± 0.10, n = 24). The most

371   significant Os$_i$ fluctuations within the INI, including the minimum and maximum values of 0.25

372   and 1.07, respectively, are recorded near the PTB (Fig. 3k). Within the lower sampling resolution

373   for our nitrogen analyses, total N contents seem to correlate with TOC contents (Fig. 3l; compare

374   to Fig. 2h). The δ^{15}N decreases from ~3.5–4.5‰ in the INI to ~3‰ in the SPI (Fig. 3n). Hg

375   contents are similar in the INI (67 ± 23 ppb, n = 23) and most of the SPI (63 ± 15 ppb, n = 20).

376   However, elevated Hg reaching up to 260 ppb are detected slightly (first 10-15 cm) above the

377   base of the SPI (Fig. 3c).

378

379   **5. Discussion**

380   **5.1. A (dis)continuous sedimentary record**

381   The Inertinitic-Sapropelic boundary has previously been placed at 1980.95 m core depth,

382   roughly in the middle of a continuous Upper Permian-Lower Triassic section (Thomas et al.,

383   2004; Thomas and Barber, 2004). However, subsequent studies interpret the lithological and

384   sharp geochemical changes across this boundary, and the lack of basal Triassic fossils as

385   possibly representing a stratigraphic break spanning parts of the latest Permian and possibly the

386   earliest Triassic (Grice et al., 2005a; 2005b; Metcalfe et al., 2008; Gorter et al., 2009). Although

387   erosional breaks in the Hovea-3 well are not clearly indicated by dipmeter or seismic data,

388   additional wells from the Perth Basin do show a clearly defined unconformity between the SPI

389   and INI (Gorter et al., 2009). Our data further outline the contrasting geochemical characteristics

390   of the two main intervals (Figs 2 and 3) and support the presence of an erosional or non-

391   depositional hiatus. For example, Os$_{initial}$ ratios, biomarker ratios and HIs are remarkably

392   sustained throughout each interval, but are clearly different between the two intervals. Therefore,

393   these end-member values can be used to evaluate stratigraphic continuity across a densely

394   sampled boundary. During continuous sedimentation, even in rapidly changing conditions, we

395   would expect a gradual shift across the transition between the two intervals. Instead, we observe

396 a relatively sharp shift, with five samples from the boundary interval displaying mixed

397 geochemical signals without a systematic mixing trend (Fig. S4). These characteristics are more

398 akin to an erosional boundary between the two intervals, with the mixed, ~8-cm-thick boundary

399 zone representing sedimentary reworking. Further evaluation based on both organic and

400 inorganic evidence supports the seemingly random mixing relations in the boundary layer (Fig.

401 S5); the five samples defining this mixed layer are excluded from further discussion and

402 evaluation of geochemical correlations.

403 **5.2. Depositional age**

404 Identification of stage and sub-stage boundaries and international calibration of the PTB

405 Interval in Australian sections in general, and in the Perth Basin in particular, is hindered by the

406 lack of marine index fossils, the endemic nature of Australian flora and fauna, paucity of precise

407 radio-isotopic ages, and lack of unequivocal chemostratigrapy and magnetostratigraphy (Foster

408 et al., 1998; Metcalfe et al., 2008). Prior to this study, radiometric dates for P–Tr sections in

409 Western Australia, including Hovea-3, were not available.

410 *5.2.1. Biostratigraphic constraints*

411 The chronostratigraphy of the Hovea Mb is based on palynology and supported by relatively

412 sparse Permian brachiopods and Triassic bivalve macrofossils (Fig. 1c; Thomas et al., 2004).

413 According to Thomas et al. (2004), the SPI is within the *Kraeuselisporites saeptatus* biozone

414 (Griesbachian-Smithian based on correlation with the Salt Range in Pakistan). The INI ranges

415 from upper parts of *Dulhuntyispora parvithola* biozone (Wordian-Wuchiapingian) to the

416 *Protohaploxypinus microcorpus* biozone (Changhsingian). The highest *P. microcorpus*

417 assemblage is at 1981.0 m and the lowest *K. saeptatus* assemblage is at 1980.85 m core depth. In

418 addition to palynology, two bivalve macrofossil species from the genus *Claraia* are described in

419 the SPI: *C. stachei* (found in basal Triassic sections globally), and *C. perthensis* (local species

420 closely related to *C. griesbachi*) indicate a Griesbachian age for this assemblage and support the

421 palynology data (e.g., Foster et al., 1998, Thomas et al., 2004). Further, two assemblages of

422 Changhsingian brachiopod fossils have been found in the IN I. The lower assemblage of

423 probably early Changsinghian age at 1987.38-1987.40 m depth includes two productid

424 brachiopods (*Marginifera sp. nov.* and *Austritusinia sp. nov.*) with some smaller and less

425 diagnostic specimens of probably *Cimmeriella*, *Etherilosia* and *Stenosciama*, and fragments of

426 athyrids, elythids and transverse spiriferids (Thomas et al., 2004). Up-section, an impoverished

427 assemblage with rare specimens of productid *Pinomarginifera sp*. at 1984.60 and 1984.54 m

428 depth indicates a mid-Changhsingian age (Fig. 1c; Thomas et al., 2004).

429   Additional diagnostic fossils recovered from the Hovea Mb from the Corybas 1 drill core

430 located 13 km from the Hovea-3 drill core led to some age revisions (Fig. 1c; Metcalfe et al.,

431 2008). Using larger samples, these authors recovered limited in number, but age-diagnostic

432 conodont elements. *Clarkina jolfensis* Kozur from the lowermost part of the SPI can be

433 correlated to the *C. yini–C. zhangi* Zone of Iran and Transcaucasia and therefore indicates a late,

434 but not latest, Changhsingian age. Based on the new evidence, Metcalfe et al. (2008) place the

435 PTB within the lower parts of the SPI, and not at the boundary between the SPI and INI (as in

436 Thomas et al., 2004). However, we note that the sample from the SPI containing the age-

437 indicative conodont is at the boundary with the Inertinitic Interval, and, as such, there is perhaps

438 a possibility for entrainment of fossils from a mixed boundary layer. Up-section in the Corybas-1

439 core, samples from the upper part of the SPI contain *Neospathodus dieneri* Sweet, and

440 fragmentary elements of *Clarkina sp*. and *Neospathodus sp*. that cannot be identified at the

441 species level, but together suggest an early Dienerian to Smithian age. Conodonts from the basal

442 limestone overlying the SPI (limestone marker) are also dated as Dienerian-Smithian by the *N.*

443 *dieneri–N.pakistanensis* Zones (Metcalfe et al., 2008).

444   *5.2.2. Re-Os ages*

445   The radioactive decay of ^{187}Re to ^{187}Os with time provides the basis for Re-Os

446 geochronology (e.g., Stein, 2014). Organic-rich sediments have typically high Re and Os

447 contents compared with most other rocks, as both metals are sequestered from seawater through

448 reductive accumulation in oxygen-deficient waters (e.g., Yamashita et al., 2007). Consequently,

449 a Re-Os isochron for a suite of shale samples can yield the depositional age of the shale.

450   Re-Os regressions for Hovea-3 shale intervals are shown in Table 1. Although individual

451 samples show broadly linear relations in the isochron space (Figs S7 and S8), the age

452 uncertainties are generally larger than for well-constrained Re-Os isochrons (e.g., Georgiev et al.,

453 2017). Only samples at the top of the INI yield a more precise Re-Os age of 253.5 ± 1.4 Ma (Fig.

454 4), which represents the first radiometric age from Western Australia Permian–Triassic sections.

455 Our Re-Os age confirms the biostratigraphic constraints for a Changhsingian age of the upper

456 INI (Thomas et al., 2004; Metcalfe et al., 2008). The 253.5 Ma age is consistent with a mid-

457 Changhsingian deposition, but the 1.4 Ma age uncertainty spans the entire Changhsingian stage

458 and, therefore, we cannot provide higher-resolution age constraints within the Changhsingian.

459 For perspective, magmatic zircons from ash layers within non-marine sections from Eastern

460 Australia yield U-Pb ages of ~252.2 Ma for the main P–Tr extinction event, which, similar to the

461 Hovea-3 section, occurs at the top of the *P. microcorpus* palynological zone (Metcalfe et al.,

462 2015). Therefore, this 252.5 Ma zircon age is consistent with our 253.5 ± 1.4 Ma Re-Os age for

463 the top of the INI (top of the *P. Microcorpus* zone).

464   Typically, precise and accurate Re-Os isochron ages are obtained when: 1) shales were

465 deposited in a relatively short time frame; 2) the $^{187}Os/^{188}Os$ of seawater was relatively constant

466 during shale deposition; 3) individual samples for a given isochron have variable Re/Os ratios

467 resulting in differential growth of $^{187}Os/^{188}Os$ with time; and 4) The Re-Os isotopic system

468 remained intact after deposition. Apart from the 253.5 ± 1.4 Ma Re-Os age for the top INI, the

469 remaining dated shales yield less precise Re-Os ages with 2σ uncertainties that exceed the

470 duration of P–Tr stage boundaries and limit their geochronological value (Table 1; Figs S7 and

471 S8). The narrow sample intervals combined with biostratigraphic constraints ensure that sampled

472 shales were deposited in relatively short time frames. Limited spread of Re/Os ratios can account

473 for the lower precision of Re-Os ages for the two lowermost INI (Fig. S8), but the other dated

474 intervals have relatively good spread in Re/Os values. Significant post-depositional alteration is

475 also an unlikely reason, because dated drill-core shales have high pyrite and total sulfur content

476 and low oxygen indices; these parameters are usually strongly affected upon even incipient

477 oxidative weathering (Georgiev et al., 2012). Further, unlike the weathered Permian shales in

478 Georgiev et al. (2012) that yielded entirely impossible or implausible $^{187}Os/^{188}Os$ ratios,

479 calculated initial ratios for studied samples are geologically plausible (Figs 3k and S9). These

480 arguments suggest that the lower precision of most Re-Os Hovea-3 isochrons is caused by

481 fluctuating $^{187}Os/^{188}Os$ ratios of P–Tr seawater. As such, the Hovea-3 Re-Os dataset enables

482 tracking the temporal changes in $^{187}Os/^{188}Os$ of seawater, which is affected by changes in the

483 sources that supply Os to the global ocean. This is a powerful geochemical proxy particularly

484 when compared with similar records from other P–Tr sections, as explored in section 5.4 below.

485 Global comparisons also provide further constraints on the age of the Hovea-3 section.

486 **5.3. Depositional setting, paleoredox, and oil-generation properties**

487   Constraining the depositional conditions of fine-grained sediments relies on comparison with

488 recent sediments deposited in well-characterized settings or with well-studied examples from the

489 geologic record. Redox-sensitive parameters include the degree of lamination and bioturbation,

490 trace metal contents and ratios, the amount, size and morphology of pyrite grains, the amount

491 and type of OM, and certain isotopic ratios such as δ^{34}S or δ^{15}N. The choice of paleoredox

492 proxies to be explored is critical and often determines the outcome, as single geochemical

493 indicators may sometimes yield different paleoenvironmental estimates (e.g., Tribovillard et al.,

494 2006). Ideally, a number of paleoredox proxies should be combined.

495   *5.3.1. Published constraints*

496   Previous paleoredox estimates for Hovea-3 provide conflicting results, particularly for the

497 INI. For example, Thomas et al. (2004) and Thomas and Barber (2004) argue for a well-

498 oxygenated depositional setting for this interval, based on the dominance of terrestrial OM,

499 variable bioturbation, and the presence of a high-diversity, but patchily distributed benthic

500 community. In contrast, Bond and Wignall (2010) argue for a long-term, established and stable

501 anoxic or euxinic deposition of the INI based on abundant and small (4.7–6.3 μm mean diameter)

502 pyrite framboids (examples shown in Figs S1 and S2), that are similar to framboids that form in

503 modern euxinic systems like the Black Sea (Wilkin et al., 1996). Sulfur isotope data for the INI

504 (Fig. 3b; Grice et al., 2005a; Nabbefeld et al.; 2010a) are consistent with an anoxic-euxinic

505 depositional setting. Pyrite formed in settings with unlimited sulfate supply (e.g., open system, as

506 in the water column) preserves the maximum sulfur isotope fractionation between the sulfate

507 pool and the formed sulfide/iron sulfides with a large isotope fractionation of about −50 to −60‰

508 observed in the modern euxinic Black Sea water column and surface sediments (Neretin et al.,

509 2003; Jørgensen et al., 2004). A limited sulfate re-supply during sedimentary diagenesis results

510 in higher δ^{34}S values of pyrite approaching that of the sulfate upon near-total sulfate

511 consumption (e.g., Jørgensen et al., 2004; Hartmann & Nielsen, 2012). In this respect, the low

512 δ^{34}S values of about −50‰ in the lower INI support the evidence from pyrite framboid

513 distribution for a possible pyrite formation in a euxinic water column or the associated sediment-

514 water interface.

515   Equally abundant and small pyrite framboids in the SPI (Bond and Wignall, 2002), combined

516 with fine lamination, and biomarker evidence for water column stratification (Thomas et al.,

517 2004) and surface water euxinia (Grice et al., 2005a), argue for a strongly anoxic-euxinic

518 stratified water column during deposition of the SPI. The increasing δ^{34}S values through the INI,

519 stabilizing at about −30‰ in the Sapropelic interval (Fig. 3b), at first glance seem to contradict

520 the evidence for a deposition of the SPI under euxinic conditions (see discussion below).

521 However, this $\delta^{34}S_{pyrite}$ trend may have been caused by changes in the $\delta^{34}S$ values of global

522 seawater sulfate, which sharply increase from the late Changhsingian ($\delta^{34}S_{sulfate}$ ~+10‰) into the

523 Griesbachian ($\delta^{34}S_{sulfate}$ up to ~ +25‰) (e.g., Bernasconi et al., 2017), at a relatively constant and

524 large sulfate-sulfide fractionation with a magnitude between about −50 and −60‰.

525   In the following sections, we present further new independent geochemical evidence for the

526 Hovea-3 section from major and trace element content and Rock-Eval parameters to address the

527 question of paleo-redox conditions.

5.3.2. Mineralogical controls on trace metal concentrations

529   Trace metal associations with key selected parameters reveal the main host phases for trace

530 metals in shale (organic matter, sulfides, carbonates, detrital minerals) and highlight key

531 differences between the SPI and INI (Fig. 5). Most notably, the higher carbonate contents in the

532 SPI (Fig. 2m) cause a dilution effect for most trace metals marked by ubiquitous negative

533 correlations with Ca contents (Fig. 5a); such negative correlations are absent in the INI (Fig. 5b).

534 Good correlations of Ca contents with carbonate contents and Mn, Sr, Ba, and biomarker ratios

535 in the SPI identify calcite as the main Ca-hosting phase; this is consistent with the lithological

536 description of this interval that includes frequent limestone layers and carbonate cement (Thomas

537 et al., 2004; Fig. S2). In contrast, in the INI most of these parameters (excluding Mn) do not

538 correlate with the comparatively low Ca contents, suggesting that a sizeable portion of the Ca is

539 hosted perhaps in Ca-bearing clay minerals.

540   Both intervals display significant positive Fe-S correlations (Fig. 5; Fig. S4c), suggesting that

541 most sulfur is in the form of pyrite; this is consistent with the ubiquitous presence of pyrite

542 framboids in the section (Bond and Wignall, 2010; Figs S1 and S2). It has however been shown

543 that in black shales some sulfur may also be incorporated in the OM fraction (e.g., Böttcher et al.,

544 2006, Hetzel et al., 2009). Apart from Fe, the elements correlating with S completely differ

545 between the two intervals (As, Tl, Co, Mo and Hg for the SPI compared with U, Zn Se, Pb, Re

546 for the INI. While some of these correlations may be indirect and do not necessarily imply host

547 phase relations (e.g., U with S; e.g., Morse and Luther, 1999), the differences between the two

548 intervals are obvious.

549   Positive elemental correlations with Al (a measure for the detrital clay fraction of the rock)

550 are mostly similar between the two intervals (K, Ti, Nb, Sc, Hf, Cr, Th, La, Lu), but more clearly

551 (unequivocally) expressed in the SPI. The combined set of elements correlating with Al indicates

552 that similar continental lithology supplied similar detrital material to the ocean during the PTB.

553 To these predominantly detrital elements, we can also add elements that exhibit comparable

554 positive correlations with both Al and TOC in the two intervals (V and Ag) or within the

555 Sapropelic Interval only (Cu, Zn, Se).

556   N, Os, Ni, and Ag display positive correlations with TOC among the two intervals and

557 suggest a common mechanism for enrichment within the organic matter, despite evidence for

558 contrasting properties of the organic matter in the two intervals discussed below (see also Fig. 2i,

559 j). In contrast, Hg, Tl and As correlate with TOC in the INI, and more prominently with sulfur in

560 the SPI, whereas Re and HI correlate with TOC in the SPI but not in the INI. These differences

561 in trace metal-TOC association can be attributed to the contrasting properties of organic matter

562 within the two intervals.

563   *5.3.3. Trace metal constraints*

564   Sediments in modern low-oxygen settings, including restricted basins such as the Black Sea

565 and oxygen minimum zones such as the coast off Namibia have elevated amounts of organic

566 matter, sulfur, and iron, compared with sediments deposited in normally oxygenated settings or

567 with the upper continental crust (e.g., Brumsack, 2006; Sweere et al., 2016). Enrichments in

568 redox-sensitive and sulfide (pyrite)-bound trace metals are also considered a hallmark of anoxic

569 and euxinic shales (e.g., Tribovillard et al., 2006; Brumsack, 2006; Xu et al., 2012). In this

570 respect, the elevated TOC, S and Fe contents, S/Fe and Fe/Al ratios, and calculated Fe_{py}/Fe_{total}

571 ratios (Fig. 2; Fig. S3) clearly suggest the presence of anoxic conditions during deposition of the

572 entire Hovea Mb. We emphasize that the calculated Fe_{py}/Fe_{total} ratio mentioned above is only an

573 approximation for the true Fe_{py}/Fe_{total}, because it is derived from total sulfur that likely contains

574 contributions from non-pyritic (organic- and sulfate-bound) sulfur (not measured). Comparison

575 of calculated Fe_{py}/Fe_{total} ratios with the actually measured Fe_{py}/Fe_{total} for Hovea-3 samples (Grice

576 et al., 2005a) shows excellent agreement for the SPI and some overestimation for the uppermost

577 INI (Fig. S4d), likely because of the existence of sulfate minerals (Fig. S2). Anoxic conditions

578 are further highlighted by elevated contents of the redox-sensitive metals Mo, U and Re, and

579 their elevated weight ratios with detrital-bound elements such as Al and Th (Figs 2 and 3; Fig.

580 S3). The trace metal chemistry of the SPI INI clearly differs, with two groups of redox indicators

581 showing different behaviors. S, Fe, and U contents, S/Fe, Fe/Al and U/Th ratios, and calculated

582   Fe_{py}/Fe_{total} ratios are consistently higher in the SPI, suggesting more anoxic conditions in the

583   Triassic compared with the Permian. Other redox-sensitive metals such as Mo, Se, Re, and their

584   ratios with Al are also elevated compared with average shale (e.g., Wedepohl, 1991), but

585   generally similar throughout the section. Both groups of redox indicators show a pronounced

586   peak at INI-SPI boundary, suggesting that anoxia temporarily intensified near the PTB. The

587   presence of a carbonate (Fig. 2m) peak slightly above the boundary coincides with the highest

588   Mo contents and may reflect increased alkalinity during peak anoxia; Mn concentrations (Fig.

589   S3c) follow the carbonate contents.

590   Established major element paleoredox thresholds also indicate more euxinic conditions for

591   the SPI, compared with prevailing suboxic to anoxic conditions for the INI (Fig. 2 f, g, and h). In

592   contrast, trace element proxies commonly used in the literature, such as Re/Mo, V/Cr, V/(V+Ni)

593   and Ni/Co ratios in sediments provide conflicting results (Fig. S3). Such results are often

594   observed in paleoredox studies and suggest that local factors such as the re-supply of trace

595   metals to oceanic waters, degree of basin water restriction, and surface water productivity

596   influence the trace metal contents and compromise the strict application of paleoredox thresholds

597   (e.g., Rimmer, 2004; Tribovillard et al., 2006; Hetzel et al., 2009). In these and other examples,

598   the stratigraphic changes in trace metal enrichments relative to average shale, and in diagnostic

599   metal ratios, provide more accurate paleoredox estimates. Adopting the latter approach,

600   conflicting paleoredox thresholds are reconciled with other paleoredox indicators (e.g., Fig. 2)

601   and indicate relatively more euxinic conditions for the SPI.

602   Trace metal contents also provide additional information on the depositional setting. For

603   example, the slope of linear Mo-TOC relations is sensitive to the degree of basin restriction

604   (Algeo and Lyons, 2006). Modern restricted basins like the Black Sea with limited trace metal

605   supply may exhaust their seawater Mo inventory relative quickly (hence low Mo/TOC slopes;

606   e.g., ~4.5 in Black-Sea sediments), whereas Mo is replenished more efficiently in less restricted

607   basins and these sediments preserve higher Mo/TOC slopes (e.g., ~45 for Saanich Inlet

608   sediments; Algeo and Lyons, 2006). In this respect, uniformly low Mo/TOC ratios and low

609   Mo/TOC slope of ~1.2 for the Hovea-3 sediments indicate a strong basinal restriction. Recently

610   proposed trace metal indicators for the depositional setting generally agree with this Mo/TOC

611   proxy and provide additional paleoproductivity constraints (Fig. 6). Application of the Cd/Mo

612   versus Co*Mn proxy (Sweere et al., 2016) distinguishes between the SPI (more restricted setting

613 much like present-day Black Sea sediments) and the INI (generally less restricted setting

614 resembling sediments from present-day Arabian Sea) (Fig. 6). The isotopic composition of

615 sedimentary N reflects the primary source of nitrogen to living organisms that later formed

616 sedimentary organic matter. This source and the mechanisms of N utilization depend also on the

617 depositional setting and thus can help discriminate between organic-rich sediments from

618 restricted basins (low sedimentary $\delta^{15}N$) and those from settings dominated by upwelling (high

619 $\delta^{15}N$ values; e.g., Quann et al., 2013). For example, $\delta^{15}N$ values of about +10‰ are recorded in

620 Upper Permian sediments from northern latitude settings with vigorous upwelling (e.g.,

621 Schoepfer et al., 2012; Georgiev et al., 2015a; Georgiev et al., 2015b). In contrast, the lower

622 $\delta^{15}N$ values for the Hovea-3 samples (+2.5‰ and +4.2‰; Fig. 3n) generally support a more

623 restricted depositional setting inferred from Mo/TOC and Cd/Mo trace metal proxies. Our sparse

624 data for the Triassic portion generally support the presence of globally lower $\delta^{15}N$ of Lower

625 Triassic sediments compared with Upper Permian sediments related to a switch from

626 denitrification to nitrogen fixation conditions (e.g., Sun et al., 2019).

627 Finally, we explore sedimentary provenance and the degree of hydrodynamic sorting by

628 focusing on Al, Ti and Zr. These elements are considered unaffected by water-rock interactions

629 and biological processes, and their ratios are preserved during weathering and are insensitive to

630 carbonate dilution (Garcia et al., 1994; Greber and Dauphas, 2019). Preferential sorting of zircon

631 increases the Zr/Ti and Zr/Al ratios of the sand fraction, whereas Al and Ti are dominantly clay-

632 bound and are enriched in the finer fraction. On the other hand, Ti is more compatible in mafic

633 minerals than both Al and Zr, and therefore changing Zr/Ti and especially Al/Ti ratios (less

634 affected by sorting) in sediments likely reflect changes in the eroding material that was supplied

635 to the basin. Sorting-sensitive Zr/Ti and Zr/Al ratios slightly increase up-section in the INI and

636 reach a clear maximum below the boundary at ~1981.3 m depth (Fig. S3l-m; Fig. 6b). These

637 variations suggest an increasing sand-to-clay ratio within the Inertinitic Interval (Fig. 6) and

638 indicate shallowing of the basin towards the PTB, which is consistent with the presence of an

639 erosional boundary between the INI and SPI discussed earlier. The subsequent up-section return

640 to low values in the SPI (Fig. S3l-m) is consistent with previous interpretations for deepening of

641 the basin in the Triassic (Thomas et al., 2004). We note that Al/Ti ratios are overall higher in the

642 SPI (Fig. 6; Fig. S3n), indicating increased contributions from more felsic crustal materials (Fig.

643 6b). Although the exact source of detrital material cannot be identified, these observable

644 differences in the type of eroding material present additional arguments for the presence of an

645 erosional gap between the two intervals.

5.3.4. Organic matter constraints

647 The amount and properties of the OM in the Hovea Mb are important not only as a primary

648 source for the oil accumulation in the northern Perth Basin (Thomas and Barber, 2004), but as an

649 indicator for the depositional setting of the shales. Despite similar TOC contents, the dominant

650 type of OM in the two intervals is clearly different, particularly with regards to HI. Various

651 classifications for OM type clearly discriminate between type IV in the INI and types I-II in the

652 SPI (Fig S6a, c, e and f). Types I and II OM are oil prone and dominated by hydrogen-rich algal

653 material deposited in lacustrine or, in the case of Hovea-3, marine settings. In contrast, type IV is

654 hydrogen-poor OM with no potential for hydrocarbon generation; it is derived predominantly

655 from recycled, subaerially weathered and oxidized terrestrial OM. Types I and II OM are easily

656 degraded in oxic water and, therefore, its dominance in the SPI requires anoxic or euxinic

657 depositional conditions. In contrast, type IV OM is more resistant and is deposited within

658 sediments across all depositional conditions, provided that there is a nearby source on the

659 continents supplying it to the oceans.

660 In this respect, the INI can be interpreted as deposited in an oxic environment that destroyed

661 whatever amount of algal OM was settling through the water column and thereby concentrated

662 the resistant type IV OM. However, this interpretation is at odds with the high sulfur content and

663 isotopic composition, the abundant and fine framboidal pyrite, and the trace metal redox proxies.

664 These can be reconciled if the OM preserved in the INI is considered only as the inevitable

665 background sedimentation of recycled continental material in a near-shore setting. The lack of

666 marine OM in the rock then remains a perplexing question given the general indicators for

667 anoxic conditions that favor preservation of marine OM.

668 Originally present marine OM could have been removed by post-depositional oxidation, but

669 such a process is not supported by the high sulfur contents, low OI, and overall good

670 preservation of Re-Os isotope systematics discussed below (see detailed discussion in Georgiev

671 et al., 2012). Preferential and efficient transformation of marine OM to mobile hydrocarbons

672 during burial can also account for the dominance of type IV OM in the Inertinitic Interval. Rock-

673 Eval parameters indicate a somewhat higher maturity for this interval (Fig. 2k). However, burial

674 can cause differences in T_{max} only if thick (generally few km) sediments were deposited on top

675 of the INI and subsequently removed before deposition of the SPI, which is unlikely. A different

676 response of the type IV and type I OM to heating during Rock-Eval pyrolysis provides a more

677 plausible explanation for the T_{max} differences (see also Thomas and Barber, 2004). The implied

678 maturity levels from T_{max} are not extreme and are generally consistent with peak maturity

679 generation (Fig. S4b, e) and reported vitrinite reflectance values for the Hovea Mb in general are

680 also relatively low ($\leq\sim0.7$; Thomas and Barber, 2004; Grice et al., 2005b). Combined, these

681 maturity indicators do not suggest near-complete transformation of marine organic matter.

682   Despite the general predominance of terrestrial type IV OM in the INI (50-70 % Thomas et al.,

683 2004), the remaining OM in these samples is amorphous (Fig. 2i) and while not clearly assigned

684 to continental or marine origin (Thomas et al., 2004, suggest it may be continental), perhaps

685 some of it is of marine origin. Geochemical evidence clearly supports the presence of marine

686 OM. For example, extracted organic matter from the INI has a dominantly marine signature

687 sourced from algae or cyanobacteria (Thomas et al., 2004). In addition, the $\delta^{13}C$ of extracted

688 hydrocarbons from this interval are markedly lower than $\delta^{13}C$ of bulk kerogen dominated by

689 terrestrial OM (Fig. 3a; Thomas et al., 2004; Grice et al., 2005a), supporting a marine origin for

690 these molecules. Therefore, we argue for an enhanced preservation of marine OM in the INI, and

691 explain the low HI of this interval as a mass-balance effect, where strong contributions of

692 terrestrial type IV OM in a proximal setting with high sedimentation rates overwhelm the marine

693 signal.

694   **5.4. Global Re-Os-Hg-N signals across the P–Tr boundary**

695   Vast amounts of geochemical data on P–Tr boundary sections are presented in the literature.

696 Whereas many geochemical parameters are influenced by local depositional conditions and their

697 interpretation carries local significance, some elemental and isotopic signals are identified and

698 correlated in multiple sections across the globe and provide evidence for global changes in the

699 Late Permian. Most notably, a significant drop in the $\delta^{13}C$ carbonate values, assumed to reflect a

700 major input of isotopically light volcanic carbon into the ocean, marks the LPME horizon (e.g.,

701 Shen et al., 2013). Here, we compare stratigraphic trends in Re-Os-Hg-N data observed in the

702 Hovea-3 section to similar signals in the Meishan section, South China, the Opal Creek section,

703 West Canada, and in the mid-Norwegian shelf (Fig. 7). We discuss the major similarities and

704 differences between these sections, their implication for reconstructing global processes

705 operating across the PTB, and provide additional geochemical constraints for the placement of

706 the PTB in the Hovea-3 section.

707 *5.4.1 Initial $^{187}Os/^{188}Os$ constraints*

708 Re-Os isotopes and elemental concentrations provide information about the sources

709 supplying Os to the ocean ($^{187}Os/^{188}Os$ ratios are low, ~0.127 in both juvenile oceanic crust and

710 meteorites, and higher, ~1.4 in eroding continental materials; Peucker-Ehrenbrink and Ravizza,

711 2000), about local redox conditions (anoxia results in higher sedimentary contents of both Re

712 and Os, with relatively high Re/Os ratios), and potentially, subject to tentative interpretations,

713 about increasing oceanic temperature and/or acidity (marked by increasing Re/Os ratios in

714 sediments; Georgiev et al., 2011). All sections presented in Fig. 7 are characterized by fairly

715 stable $^{187}Os/^{188}Os$ initial ratios of about 0.5-0.7 in the Late Permian, confirming the validity of

716 the sedimentary Os_i as representative for the $^{187}Os/^{188}Os$ of the Late Permian ocean. Within these

717 overall stable trends, individual samples from the Wuchiapingian (in Meishan) and pre- and post-

718 LPME Changhsingian (in Hovea-3 and Opal Creek) deviate to lower Os_i down to ~0.4 and even

719 0.20-0.25. These low values generally indicate contributions from basaltic volcanism and/or

720 meteorites and have been interpreted as increased supply of Os from the Emeishan Trap basalts

721 and the Siberian Trap basalts, respectively (Georgiev et al., 2015a; Liu et al., 2019; this study).

722 However, the geologic record contains examples of substantial magmatic influence on ocean

723 chemistry, which display sustained stratigraphic peaks of lower Os_i in marine sediments that are,

724 importantly, coupled with notable increases of sedimentary Os. For example sediments deposited

725 during the oceanic anoxic event 2 (OAE2) have low Os_i and up to 4000-6000 ppt ^{192}Os, which is

726 about 40-130 times pre-event background values for those sections (Turgeon and Creaser, 2008).

727 In contrast, the quick recovery towards higher Os_i values and the lack of notable Os enrichment

728 in the Upper Permian sediments from various sections (<100 ppt in most samples, with a

729 maximum of ~200 ppt in sediments across the Wuchiapingian-Changhsingian boundary; Fig. 7)

730 suggests that the direct contributions from Late Permian volcanism were short-lived and

731 relatively minor compared with the total oceanic Os budget. The large volume of the Siberian

732 trap basalts should have provided sufficient Os to overwhelm the oceanic budget, but the

733 continental (as opposed to submarine) location apparently prevented significant Os input to the

734 Late Permian ocean.

735   In the Hovea-3 section, the uppermost Permian samples from the interval at 1981 m depth

736 have slightly higher Os_i of ~0.65-0.90 than older Permian strata (0.53-0.74; Fig. 7). This trend

737 may reflect an increased proportion of weathered continental material with higher Os_i, which is

738 consistent with independent geochemical evidence for a higher proportion of sand over clay

739 (higher Zr/Al ratios; see Garcia et al., 1994) in the same samples relative to older Permian strata

740 (Fig. 6b). Shallowing of the basin in the latest Permian is also consistent with the speculated

741 presence of a depositional break between the INI and SPI, as discussed earlier.

742   The Permian–Triassic boundary (PTB) in both the Meishan and Opal Creek sections is

743 marked by a relatively minor drop of $^{187}Os/^{188}Os$ to ~0.45, followed by a recovery to values of

744 ~0.6 (Opal Creek) and ~1.0 (Meishan) in the Griesbachian. While there are two samples with

745 lower Os_i of ~0.3-0.5 close to the INI-SPI boundary, it is unclear whether these can be correlated

746 to other sections. The Hovea-3 section also displays a recovery of Os_i values, but unlike the

747 Meishan and Opal Creek section, higher $^{187}Os/^{188}Os$ of ~1.5 are permanently established

748 throughout the SPI (Fig. 7). This difference may indicate that regional basin restriction

749 influenced the $^{187}Os/^{188}Os$ of Hovea-3 Triassic sediments (e.g., McArthur et al., 2008), but it

750 could also stem from different sampling resolution covering different portions of the

751 Griesbachian. Importantly, the Hovea-3 section uniquely contains organic-rich Griesbachian

752 marine shales that are much more likely to preserve the primary isotope signature of Triassic

753 seawater than sediments containing almost exclusively recycled terrestrial organic matter, such

754 as in Meishan, Opal Creek, and elsewhere (see discussion in Georgiev et al., 2015a). In this

755 respect, the higher $^{187}Os/^{188}Os$ of Triassic Hovea-3 shales is consistent with postulated

756 anomalously high global weathering fluxes in the Early Triassic (Algeo and Twitchett, 2010),

757 which should have provided large amounts of continentally-derived, radiogenic Os to alter the

758 isotopic composition of the ocean.

759   The changing Os isotopic composition of sediments can be used to calculate the changing

760 weathering fluxes (e.g. Cohen et al., 2004; Bottini et al., 2012; Them et al., 2017). Similarly, we

761 calculate the changing weathering fluxes during the P–Tr transition based on the change of

762 $^{187}Os/^{188}Os$ initial ratio from 0.6 (Upper Permian sediments from Hovea-3, Greenland, Meishan)

763 to 1.5 (Lower Triassic sediments in Hovea-3). These calculations assume a constant flux of

764 mantle-derived Os of 2210 moles/year with an isotopic composition of 0.127 (present-day

765 values; Peucker-Ehrenbrink and Ravizza, 2000; Them et al., 2017), and a changing flux of

766 continentally-derived Os with of ^{187}Os/^{188}Os of 2.0 (as the present-day estimate of 1.4 is lower

767 than ^{187}Os/^{188}Os in the Lower Triassic sediments). Results, dependent on the accuracy of these

768 constraints, show that the increase in seawater ^{187}Os/^{188}Os can be achieved by an 8 times increase

769 in the flux of continental-derived Os to the oceans. These Os-isotope constraints matches the

770 average increase of weathering fluxes estimated by higher sedimentation rates in the Lower

771 Triassic sediments (7 times the Late Permian values; Algeo and Twitchett, 2010). While our

772 modeling provides only a crude estimate, any combination of reasonable inputs to this model

773 will indeed require a high increase of the weathering fluxes in the Early Triassic.

774   *5.4.2 Re/Os ratios*

775   Georgiev et al. (2011) identified anomalously high Re/Os ratios in Upper Permian shales

776 from Norway, Greenland, and elsewhere, and linked these to anoxia, oceanic acidity and

777 elevated temperatures. More recent data, including from this study, further outline the global

778 occurrence of anomalously high Re/Os ratios in the Late Permian (Fig. 7). In both Meishan and

779 Opal Creek sections, ^{187}Re/^{188}Os ratios are high in the Permian, reach the highest values in the

780 latest Permian shortly before the extinction (bed 22 in Meishan; the lowermost point in the Opal

781 Creek section), and rapidly drop to low values through the extinction (Opal Creek, potentially

782 Meishan) and into the Triassic (Fig. 7). The drop in Re/Os ratios is accompanied by a drop of

783 δ^{15}N which is significant in the Opal Creek section and visible, but less pronounced in the

784 Meishan section. The decrease of δ^{15}N in these sections is generally interpreted to reflect the

785 rapid transition from a productive upwelling setting (particularly for the Opal Creek section;

786 Shoepfer et al., 2012) with nitrogen cycling through nitrate, to a more restricted setting with

787 enhanced nitrogen fixation from cyanobacteria (Cao et al., 2009; Georgiev et al., 2015a; Sun et

788 al., 2019). In Hovea-3, Re/Os ratios follow a similar pattern, with low values <500 in the

789 Wuchiapingian, much higher values reaching ~5000 in the upper Changhsingian, and low values

790 <1000 in the Triassic. δ^{15}N values and trends in the Hovea-3 section are similar to these in the

791 Meishan section, although the drop in δ^{15}N coinciding with the drop in Re/Os ratios is more

792 subdued in Hovea-3 (Fig. 7). Trace metal evidence also support a change from upwelling to a

793 more restricted setting across the INI-SPI boundary (Fig. 6a). We note that the decrease of Re/Os

794 and δ^{15}N in the Meishan section coincides with the major decline in δ^{13}C$_{carb}$ heralding the LPME

795 (Fig. 7). Therefore, our global comparisons of the Re/Os patterns alone, or in combination with

796   the initial Os and N isotopic constraints, suggest that the entire SPI was deposited after the main

797   extinction event and likely entirely within the Griesbachian.

798   The exact mechanism controlling Re/Os ratios remains unclear, but our new data provide

799   some important new constraints. Clearly, anoxia alone cannot account for the increasing Re/Os

800   ratios, as the SPI with low Re/Os ratios records more anoxic conditions than the Upper Permian

801   INI; Triassic Opal Creek sediments are anoxic (Georgiev et al., 2015a) but have low Re/Os ratios.

802   Similarly, global warming alone cannot account for anomalous Re/Os ratios of uppermost

803   Permian sediments, as the Early Triassic climate was substantially hotter than the Late Permian

804   (Sun et al., 2012). In all studied sections, anomalous Re/Os ratios seem to be related to

805   increasing Re and relatively invariable Os in the sediments (Fig. 7). Therefore, Re enrichments

806   and high Re/Os ratios in Upper Permian are related either to increased Re over Os supply (e.g.,

807   from acid volcanism) and/or enhanced sequestration of Re (and a constant for Os) in the Upper

808   Permian sediments (perhaps related to oceanic acidity; Georgiev et al., 2011). Alternatively, the

809   elevated Re contents and Re/Os ratios could be a direct consequence of geographically

810   widespread but currently unknown biological affinity for Re, either by direct incorporation in

811   living organisms during the Late Permian, or through early diagenetic microbial activity. In the

812   aftermath of the LPME, extinction of the organisms responsible for this enrichment could have

813   caused a decrease of Re/Os ratios to values more typical for sediments. While these alternatives

814   cannot be precisely evaluated, our new data clearly establishes global and major synchronous

815   changes in the Re/Os ratios of Permian–Triassic sediments that can be used for global

816   correlations and perhaps hold important clues for what caused the LPME.

817   For example, we note that the incomplete Re/Os record in Meishan seems to correlate with

818    $\delta^{13}C_{carb}$, with low Re/Os ratios corresponding to low $\delta^{13}C_{carb}$ and vice versa. (Fig. 7a). The

819    $\delta^{13}C_{carb}$ values in Meishan drop from ~ +4‰ to ~ −3‰ - −4‰ across the LPME horizon. If we

820   view the entire Changhsingian stage as a time of major positive $\delta^{13}C_{carb}$ disturbance from values

821   of about −2 to 0‰ in the Wuchiapingian to values of +3 to +4‰ lasting through most of the

822   Changhsingian, we can offer a somewhat alternative view on the classically invoked LPME

823   scenario. Positive $\delta^{13}C_{carb}$ shifts can result from massive organic carbon drawdown into organic-

824   rich sediments, which sequester isotopically light organic carbon and enrich the remaining

825   dissolved carbonate pool.

826

827   The negative $\delta^{13}C_{carb}$ shift at the LPME is often interpreted as being caused by massive

828 addition of CO_2 to the atmosphere directly degassed from the Siberian Trap basalts, and, more

829 importantly, released by thermal metamorphism of carbonates and organic-rich shales during the

830 emplacement of Siberian Trap sills (Svensen et al., 2009; Burgess et al., 2017). However, if the

831 LPME was caused not by these massive amounts of CO_2 injection, but through another

832 mechanism that greatly reduced biological production, the negative $\delta^{13}C_{carb}$ values in the latest

833 Permian and earliest Triassic can be viewed mostly as a return to normal, pre-Changhsingian

834 conditions. In this case, at least half of the LPME $\delta^{13}C_{carb}$ negative shift (from +4 to ~ 0 to −1‰)

835 can be assigned to collapse of biological production and limited export of organic carbon to

836 sediments, which in turn would require smaller amounts of CO_2 emissions from volcanism. In

837 fact, numerical modeling of this process, with inevitable assumptions subject to later criticism,

838 suggests that the collapse of primarily productivity can cause the entire isotopic shift at the

839 LPME (Rampino and Caldeira, 2005). In the marine realm, this can be achieved by widespread

840 anoxic conditions reaching the photic zone and permanently damaging most aerobic primary

841 producers. Evidence for photic zone euxinia is reported from many Upper Permian sections,

842 including Hovea-3 (e.g., Grice et al., 2005a; 2005c; this study), Meishan (Cao et al., 2009), West

843 Canada (Hays et al., 2007), and East Greenland (Grice et al., 2005a). Widespread euxinia would

844 have been particularly damaging during times of sea level fall during the LPME because of the

845 associated restriction of biologic habitats. Eruption of the Siberian Traps could have provided the

846 final blow (e.g., the second scenario of Bowring et al., 1998). Compilations in Knoll et al. (2007)

847 based on Sepkoski (2002), show a major decline in biodiversity throughout the Late Permian,

848 and the biodiversity data in Jin et al. (2000) confirm that about half of the Changhsingian marine

849 genera in South China permanently disappear from the record *before* the LPME. Perhaps the

850 final blow likely related to the Siberian Traps eruption was so effective only because

851 Changhsingian life was already significantly reduced in numbers, and with the survivors adapted

852 to unusual conditions.

853   *5.4.3 Mercury content and isotope composition*

854   Elevated sedimentary Hg contents and Hg/TOC ratios in the geologic record are often

855 associated with emplacement of large igneous provinces, and provide a tool for identification of

856 volcanic inputs of Hg and for global correlations across the PTB (e.g., Grasby et al., 2017; Scaife

857 et al., 2017; Shen et al., 2019a; Wang et al., 2019; Sial et al., 2020). Importantly, distinct peaks

858 in Hg contents and derived Hg/TOC ratios up to 2–8 times their background values are detected

859 near the PTB, at or shortly after the LPME horizon, in about 20 marine sections worldwide (e.g.,

860 Grasby et al., 2017; Shen et al., 2019a; Wang et al., 2018; Wang et al., 2019) and in terrestrial

861 PTB sections (e.g., Shen et al., 2019b). These generally coeval peaks are thought to reflect Hg

862 injection in the atmosphere directly through volcanic eruptions or through sill emplacement

863 releasing Hg from heated organic-rich host rocks (e.g., Grasby et al., 2017). Analyses of Hg

864 enrichment profiles from multiple sections worldwide reveal a characteristic relation of the Hg

865 peak to the paleogeographic location of the section and to paleo water-depths, which are

866 consistent with volcanogenic input of Hg to the atmosphere, and inconsistent with increased

867 supply of Hg to the ocean by terrestrial runoff (Shen et al., 2019a). The substantial Hg input to

868 the atmosphere was followed by a rapid (<2–1000 years) Hg adsorption onto sinking organic

869 matter and ultimately into sediments (Shen et al., 2019a). As such, Hg and Hg/TOC peaks

870 provide a rare geochemical proxy for the direct involvement of the Siberian Trap magmatism in

871 the Late Permian. The levels of Hg enrichments and Hg/TOC peaks can also reflect increased

872 supply of terrestrial Hg (Them et al., 2019), or incorporation of atmospheric-derived Hg into

873 sulfides precipitating in the water column or at the sediment-water interface (Shen et al., 2019c).

874 These two processes are not necessarily related to volcanic inputs, but rather to increasing

875 continental runoff or intensifying anoxia, respectively (Them et al., 2019; Shen et al., 2019c).

876 These two scenarios require additional evaluation based on elemental relationship (Hg-TOC-Al-

877 S), and on the Hg-isotopic constraints (e.g., Jones et al., 2019; Them et al., 2019; Shen et al.,

878 2019c)

879 Data from the Hovea-3 section define two closely spaced peaks of Hg contents and Hg/TOC

880 ratios entirely within the basal SPI (Fig. S4e, f). Samples above the INI-SI boundary between

881 1980.94 and 1980.89 m depth contain elevated Hg contents between 133 and 213 ppb Hg. The

882 second Hg peak is ~6 cm further up-section and ~15 cm above the INI-SI boundary. Within a

883 narrow 3-cm-thick interval (1980.825-1980.790 m depth), Hg contents reach 260 ppb and

884 Hg/TOC ratios reach ~100 (ppb/wt%) (Fig. 7; Fig. S4e, f). These enrichment levels are about 4–

885 7 times higher than the overall pre- and post-enrichment background (Fig. 7), which is similar to

886 Hg enrichments in other PTB sections. Samples defining the first Hg peak belong to the mixed

887 boundary zone and may be affected by sedimentary reworking (see earlier discussion and Fig.

888 S4). The samples defining the second Hg peak, however, are not affected by such processes and

889 are generally indistinguishable from most other SPI sediments except for their Hg characteristics.

890 As a whole, Hg contents of studied samples do not correlate with Al contents (Fig. 5), suggesting

891 that supply of terrestrial mercury through increased runoff was not key. In contrast, Hg contents

892 correlate positively with both TOC and S, with better Hg-TOC correlations in the INI and better

893 Hg-S correlations in the SPI. Samples defining the second Hg peak are indeed sulfur rich (3.8-

894 5.8 wt%) and may suggest a strong Hg complexation with sulfides during anoxia and without the

895 need for volcanogenic inputs, as described for Ordovician black shales (Shen et al., 2019).

896 However, despite these good Hg-S correlations (Fig. 5a), other S-rich samples from the

897 Sapropelic Interval (e.g. at 1970 m depth, with more than 4 wt% S) do not show elevated Hg or

898 Hg/TOC ratios (Fig. 3). Therefore, we suggest that the peak in Hg contents and Hg/TOC ratios

899 likely reflects volcanic inputs; Hg-isotopic evidence further supports this conclusion. Importantly,

900 as for all other SPI samples, the second Hg peak occurs in sediments with high TOC contents

901 that contain predominantly marine organic matter, as indicated by their high HI of 350–470 mg

902 hydrocarbons/g TOC (Fig. S4). Therefore, we conclude that the second Hg loading peak clearly

903 characterizes marine conditions close to the PTB.

904   The same cannot be confidently inferred for many other marine sections, including the

905 Meishan and Opal Creek sections presented in Fig. 7, which often have lower-TOC values

906 comprised predominantly of terrestrially-derived reworked OM marked by low HI <100 mg

907 hydrocarbons/g TOC (HI for Meishan and Opal Creek are given in Shen et al., 2011 and

908 Georgiev et al., 2015b, respectively). Lack of evidence for terrestrial Hg input during the Hg

909 peaks in Hovea-3 suggests a strong and relatively short-lived input of volcanogenic Hg near the

910 base of the SPI. Global comparisons show that the Hg peak occurs close to the LPME in all

911 studied sections (e.g., Wang et al., 2018; Shen et al., 2019a), and, therefore, we can infer the

912 same for the Hovea-3 section. However, a more detailed analysis of temporal trends of Hg

913 enrichments in numerous PTB sections reveals small variations in the relative timing of the Hg

914 peak with respect to both the LPME and PTB (Wang et al., 2018; Shen et al., 2019a); these

915 variations limit the exact placement of the LPME horizon in the Hovea-3 section based on Hg

916 enrichments. It is possible that most of these variations result from slightly different age models

917 for the different section and uncertainties related to the exact placement of the LPME, and that if

918 these are refined, the Hg peak is truly synchronous with the LPME event globally (Shen et al.,

919 2019a). If that is the case, then the LPME horizon in the Hovea-3 section is at 1980.8 m depth,

920 near the base of the SPI. Additional Hg data for the Hovea-3 section support the presence of a

921 Hg and Hg/TOC peak at the INI-SPI boundary, and include a single sample at ~1984 m depth

922 with high Hg and Hg/TOC ratios (Sial et al., 2020; see Fig. 7). Although we did not sample at

923 exactly the same depth, our samples from neighboring vertical intervals near 1984 m core depth

924 show elevated Hg/TOC ratios and a clear peak of Hg/S ratio. If this level is correlative with the

925 globally expressed Hg/TOC peaks, then the LPME in the Hovea-3 section is located within the

926 INI. However, this placement of the LPME is generally not supported by the available

927 biostratigraphy (see section 5.1) and by the otherwise geochemically uneventful horizon at 1984

928 m depth – most geochemical changes occur about 3 meters upsection (Figs. 2 and 3). The

929 Hg/TOC and Hg/S peak at the 1984 m interval can be produced either by increased volcanic

930 input in the pre-extinction Changhsingian, or by increased contributions of terrestrial Hg from

931 continental runoff. The latter scenario is consistent with the predominance of terrestrial organic

932 matter in the INI in general, but volcanic contributions cannot be excluded.

933 The isotopic composition of mercury provides further constraints on Hg sources and

934 depositional pathways. Mercury has a complex biogeochemistry, with multiple physical,

935 chemical, and biological processes inducing both mass-dependent fractionation of stable Hg

936 isotopes (MDF, usually reported as δ^{202}Hg), and mass-independent isotopic fractionation (MIF)

937 of even-numbered and more commonly of odd-numbered Hg isotopes (usually reported as

938 Δ^{199}Hg) (Blum et al., 2014). The two main sources of Hg to the oceans are through continental

939 runoff and through atmospheric deposition; their isotopic composition is briefly summarized

940 below based on an extensive literature review (Blum et al., 2014; Grasby et al., 2017; Zheng et

941 al., 2018; Wang et al., 2018; Shen et al., 2019a; Shen et al., 2019b; Wang et al., 2019; and

942 references therein). Volcanic emissions of elemental gaseous Hg^0 (δ^{202}Hg of −1.4‰ to −2.1‰)

943 and particulate Hg^{2+} (δ^{202}Hg of ~ 0‰ to −0.2‰) dominate non-anthropogenic sources to the

944 atmosphere. Atmospheric Hg enters terrestrial and marine systems through direct uptake by

945 plants, absorption, or through oxidation to Hg^{2+} species. During this step, various kinetic

946 reactions impart a large MDF: modern foliage, soils, and coal deposits generally have more

947 negative δ^{202}Hg (−2‰ to −4‰) than atmospheric Hg. Consequently, trends to more negative

948 δ^{202}Hg values can be interpreted as an indication, but not as a unique signal, of increasing

949 terrestrial runoff (e.g., Grasby et al., 2017). Volcanic emissions provide Hg with little to no MIF

950 (Δ^{199}Hg ~0‰). Subsequent photochemical reduction of Hg^{2+} and methyl-mercury in the

951 atmosphere imparts a small negative MIF to the products (Hg^0), which is taken up terrestrial

952 plants and causes slightly negative $\Delta^{199}Hg$ of continental plants, coals, soils, and sediments. The

953 isotopically heavier residual pool of Hg^{2+} in the atmosphere eventually enters the oceans and

954 causes a positive $\Delta^{199}Hg$ of marine organisms and thus a small positive $\Delta^{199}Hg$ of marine

955 sediments. This process is further complicated by additional photochemical reduction on part of

956 the oceanic Hg^{2+}, which produces positive MIF in the remaining Hg^{2+} oceanic pool when Hg^{2+} is

957 bound to oxygen (e.g., normally oxygenated waters), and negative MIF when Hg^{2+} is bound to S

958 (e.g., during photic-zone euxinia) (Zheng et al., 2018). At times of increased volcanic input

959 primary volcanic signatures ($\Delta^{199}Hg$ ~0‰) are expected to dominate the atmospheric Hg

960 composition, and marine sediments deposited during these events will likely carry a similar

961 isotopic signature of $\Delta^{199}Hg$ ~0‰.

962   In Hovea-3, we observe strong signals of MDF of Hg. A general decrease of $\delta^{202}Hg$ is noted

963 in the INI from ~−1.2‰ in the Wuchiapingian to ~−2.0‰ in the mid-Changhsingian; this trend

964 is coupled with stable to slightly increasing Hg contents and Hg/TOC ratios (Fig. 7). Upsection,

965 the uppermost 4 m of the INI (1984 to 1981 m depth) have a similar range of $\delta^{202}Hg$ (−1.0‰ to

966 −2.4‰), with lower values towards the INI-SPI boundary. With few exceptions, $\delta^{202}Hg$ in the

967 SPI (−0.8 to −1.4‰) is similar to $\delta^{202}Hg$ in the Wuchiapingian portion of the section. Combined,

968 these stratigraphic variations strongly resemble $\delta^{202}Hg$ profiles from other PTB sections,

969 including Meishan (Fig. 7). The Guryul Ravine section in Indian Kashmir also shows the most

970 negative $\delta^{202}Hg$ close to the LPME (Wang et al., 2019). These negative values can be caused by

971 increased terrestrial runoff in the latest Permian, although such interpretation is contentious

972 (Grasby et al., 2017). Importantly, all sediments defining the second Hg and Hg/TOC peak near

973 the base of the SPI have consistently high $\delta^{202}Hg$ between −0.8‰ and 1.1‰, which is

974 inconsistent with a terrestrial source of Hg. The entire SPI also contains predominantly marine

975 organic matter with high hydrogen indices, and was deposited during deepening of the basin

976 where less runoff is expected (also see Fig. 6b). The Hg peak is expressed within a lithologically

977 and geochemically monotonous deeper-water marine section. Therefore, the Hg loading event in

978 Hovea-3 is clearly not related to increased terrestrial runoff (or to coal combustion), but instead

979 is more consistent with a volcanic Hg MDF signature. The deep-water Panthalassa Gujo-

980 Hachiman section (Japan) shows a similar change toward higher $\delta^{202}Hg$ during the Hg-peak

981 interval (Shen et al., 2019a). Hg peaks in relatively deep-water sections from equatorial

Neotethys also display relatively high δ^{202}Hg values (Wang et al., 2018), whereas in shallower Tethyan sections like Meishan the association of the Hg peak with higher δ^{202}Hg values is less clear (Grasby et al., 2017; Shen et al., 2019a) likely because of increased Hg supply from the continent.

In contrast to MDF, MIF is subdued in the Hovea-3 section. The mean Δ^{199}Hg of the Inertinitic Interval is 0.02 ± 0.04‰ (1SD, n = 19); these small variations cannot be resolved within uncertainties. The basal portion of the SPI has a similar MIF signal, with the samples defining the Hg peak having slightly more negative Δ^{199}Hg (-0.03 ± 0.03‰, n = 4). A notable change is recorded upsection in the SPI, where samples from the 1976 m and 1970 m depth intervals have consistently higher Δ^{199}Hg (0.16 ± 0.09‰, n = 5). Most, but not all, other marine PTB sections generally record variably positive Δ^{199}Hg between 0.05‰ and 0.20‰ in pre-extinction strata, a drop to near-zero or slightly negative values at the LPME and associated Hg loading peak, and near-zero to slightly positive Δ^{199}Hg in the Triassic (e.g., Meishan section, Fig. 7). The Δ^{199}Hg of ~0‰ in the INI and basal SPI is generally consistent with a volcanic source of Hg (e.g., Grasby et al., 2017; Wang et al., 2019), but such MIF signals can also represent mixing between atmospheric Hg (slightly positive Δ^{199}Hg) and terrestrially-derived Hg (slightly negative Δ^{199}Hg). Higher Hg supply from terrestrial runoff contributing organic matter with negative Δ^{199}Hg may explain the somewhat lower Δ^{199}Hg (0.02 ± 0.04‰) of the INI compared with contemporaneous sediments from other sections where positive Δ^{199}Hg (and negative MDF) are thought to reflect a dominant atmospheric Hg deposition pathway (e.g., Shen et al., 2019a). However, such a mechanism is not applicable to the SPI, which is dominated by marine organic matter. This includes sediments defining the second Hg peak, which have consistently lowest Δ^{199}Hg of -0.03 ± 0.03‰ and high δ^{202}Hg between -0.8‰ and 1.1‰. Combined, the MIF and MDF signatures of this Hg peak interval are consistent with a major input of volcanic Hg to the atmosphere, which overwhelmed the typical atmospheric Hg isotopic composition and was ultimately recorded in ocean sediments. Very similar patterns of Hg enrichment and MDF and MIF signatures are recorded near the LPME in other sections, including deep-water Panthalassa Gujo-Hachiman in present-day Japan (Shen et al., 2019a). Thus, the southern paleogeographic location of the Hovea-3 section (Fig. 1) in combination with the Hg data confirm the global geographic extent of massive volcanic Hg emissions around the LPME. Upsection, the positive Δ^{199}Hg of 0.16 ± 0.09‰ in the remaining SPI are generally consistent with a steady atmospheric

1013 deposition of Hg. Samples from the 1984 m level within the INI with elevated Hg/TOC and

1014 Hg/S ratios display comparatively high δ^{202}Hg and low comparatively low Δ^{199}Hg, with values

1015 nearly identical to the well-defined Hg peak at the base of the SPI (Figs. 3 and 7). Unlike the

1016 peak in the SPI, the peaks at 1984 m occur in an interval dominated by terrestrial organic matter,

1017 and therefore the source of Hg enrichments in this level remains unclear. Finally, we note that

1018 the differences in the Hg-isotopic data between multiple PTB sections are relatively small,

1019 particularly considering the small variations in Δ^{199}Hg. Some of these differences are easily

1020 attributable to different sampling resolution, variable lithologies, and especially to variable

1021 terrestrial runoff between the sections. In this respect, the Hovea-3 section, and especially the

1022 entire SPI that contains the Hg peak, is particularly well-suited for Hg-isotopic studies as it

1023 contains abundant Hg, and abundant marine-dominated organic matter. Therefore, Hg contents

1024 and isotopic composition of the Hovea-3 SPI directly track changing sources of Hg and

1025 depositional pathways for Hg enrichment in the Late Permian-Early Triassic world.

6. Conclusions

1027 The Hovea-3 section in Western Australia presents a near-complete marine sedimentary

1028 record through Upper Permian and Lower Triassic strata. A general trend of deepening of the

1029 basin from the Late Permian (shallow marine Inertinitic Interval, INI) into the Early Triassic

1030 (deeper marine Sapropelic Interval, SPI) was interrupted by shallowing and an inferred

1031 depositional hiatus near the Permian–Triassic boundary (PTB) related to a relatively short-lived

1032 sea-level fall. The entire Hovea-3 Mb was deposited during established oceanic anoxia and

1033 euxinia, but the more proximal setting of the lower (Wuchiapingian-Changhsingian) INI caused

1034 higher continental runoff and predominance of terrestrial over marine organic matter. In contrast,

1035 predominantly marine organic matter with a distinctive trace elemental association is recorded in

1036 the overlying SPI (entirely or predominantly Griesbachian). After a temporal intensification of

1037 anoxia near the boundary between the two intervals, generally more anoxic conditions, including

1038 photic zone euxinia, are recorded in the SPI.

1039 A Changhsingian Re-Os age of 253.5 ± 1.4 Ma for the uppermost INI confirms existing

1040 biostratigraphic estimates, and regional correlations with more precisely dated strata from East

1041 Australia further constrain this age to latest Changhsingian (close to the LPME and PTB). The

1042 contrasting properties of the OM in the INI and SPI combined with their distinct elemental and

1043   isotopic signatures suggest that the Late Permian mass extinction (LPME) likely occurred at the

1044   boundary between the two intervals, or during the depositional hiatus.

1045   Global correlations of Re-Os, N and Hg isotope compositions reveal distinct patterns,

1046   including anomalously high Re/Os sedimentary ratios during the late Changhsingian. Marked

1047   perturbations of the Hg, Re-Os, and N isotopic compositions coincide with the known decrease

1048   of $\delta^{13}C_{carb}$ and the LPME. Evidence from Os elemental isotopic data suggests relatively

1049   insignificant and certainly short-lived magmatic contributions into the pre-extinction Late

1050   Permian ocean compared with other major magmatic events during Earth history, a likely

1051   artefact of the mode of emplacement of the Siberian Traps (continental for the Siberian Traps

1052   compared with submarine for most other large igneous provinces). Consistently higher initial Os

1053   isotopic ratios in the Triassic strata from Hovea-3 confirm elevated global weathering rates in the

1054   aftermath of the extinction. We estimate that continental runoff in the Early Triassic was about 8

1055   times higher than in the Late Permian based on moderately conservative assumptions for end-

1056   members contributing Os to the P−Tr ocean. Notable isotopic perturbations at the INI-SPI

1057   boundary in Hovea-3 include an increase of Os initial ratios, decrease of $\delta^{15}N$, and the most

1058   negative $\delta^{202}Hg$. None of these, however, are clearly directly related to increased magmatic

1059   inputs, but rather signify more anoxic conditions and increased terrestrial runoff close to the PTB.

1060   Moderately elevated Hg/TOC ratios within the INI at about 1984 m depth may be related to

1061   volcanic inputs, but can also represent sizeable terrestrial Hg contributions. Increased volcanic

1062   contributions of Hg to the lower parts of the SPI are clearly outlined by a prominent peak of

1063   sedimentary Hg contents and Hg/TOC ratios, and mass-dependent and mass-independent Hg

1064   isotopic fractionation consistent with a volcanic Hg origin. However, this clear evidence for

1065   volcanic contributions is recorded above the major geochemical changes in the Hovea-3 section,

1066   within deeper-marine sediments of seemingly monotonous composition that are clearly not

1067   influenced by terrestrial runoff. As such, the location of the Hg peak in Hovea-3 section suggests

1068   that either Siberian Trap volcanism was not the major cause for the extinction, or that evidence

1069   for the Siberian Trap magmatism was erased from the Hovea-3 record during the purported

1070   stratigraphic break at the INI-SPI boundary.

1071

1072   **Author contributions**

1073 HS and JH designed the project together with KG and SG. KG provided access to drill core

1074 samples and HS selected drill core intervals for this study. GY and SG prepared shale samples

1075 for analyses. Samples were analyzed by GY (Re-Os, set 1), SG (Hg contents, set 1), CC (Hg

1076 isotopes), MEB (Hg, N, and TOC contents, set 3; major and trace metals, set 4), KG (trace

1077 metals, set 2), AIH (biomarkers, set 1), ST (major and trace metals, set 3), HJS, JLH, and SS

1078 (SEM work). SG wrote the paper with help and input from all coauthors. All authors agreed

1079 about the publication of the final manuscript version.

1080

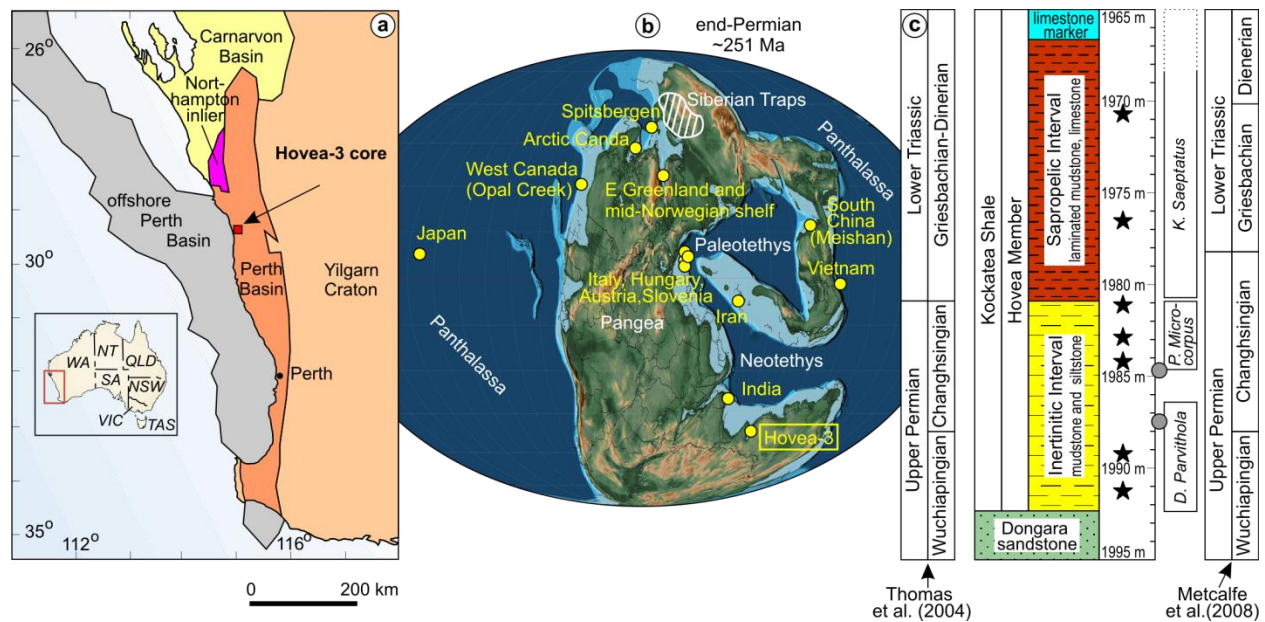1094

1095 **Figure Captions:**

1096

Figure 1. Present-day position, Late Permian location, and general litho-and bio-stratigraphy of the Hovea-3 core, showing the Intervals sampled in this study. Panel (a) shows the main geologic units in southwestern Australia and the position of the Hovea-3 core within the onshore North Perth Basin (map modified from Volk et al., 2014; Department of Water, 2017). Panel (b) shows a paleogeographic reconstruction of the Permian–Triassic world with approximate locations of the Siberian Traps (striped area) and the main studied marine Permian–Triassic boundary (PTB) sections, including the Hovea-3 core (base map modified from Scotese, 2014). Panel (c) shows the litho- and biostratigraphic subdivision of the Hovea-3 core across the PTB (modified from Thomas et al., 2004). Black stars mark the Intervals studied here; gray circles mark the location of diagnostic mid-Changhsingian and early Changhsingian fauna (Thomas et al., 2004). The rightmost columns show an alternative chronostratigraphic subdivision of the Hovea Member, with the P–Tr boundary located in the lowermost Sapropelic Interval (Metcalfe et al., 2008).
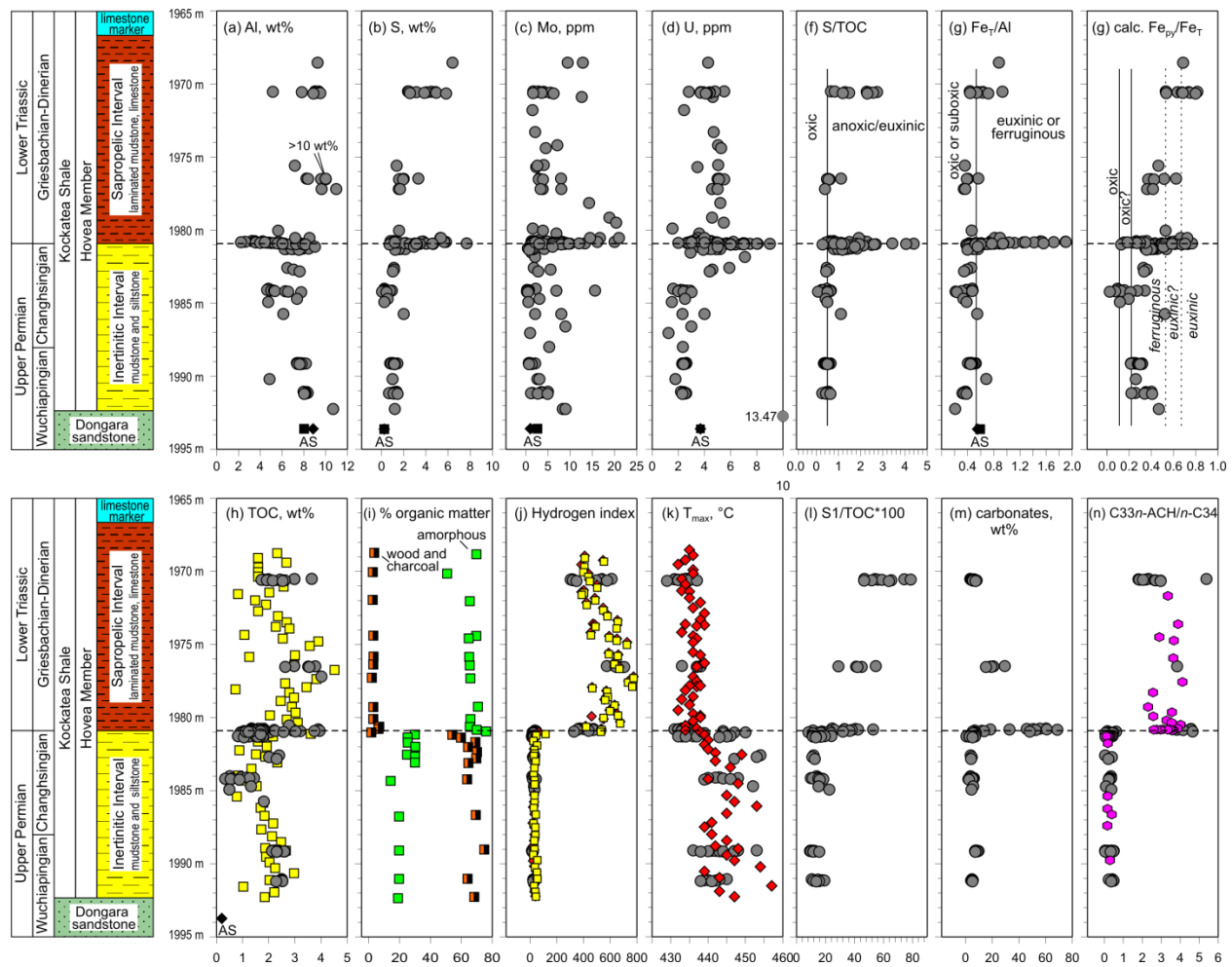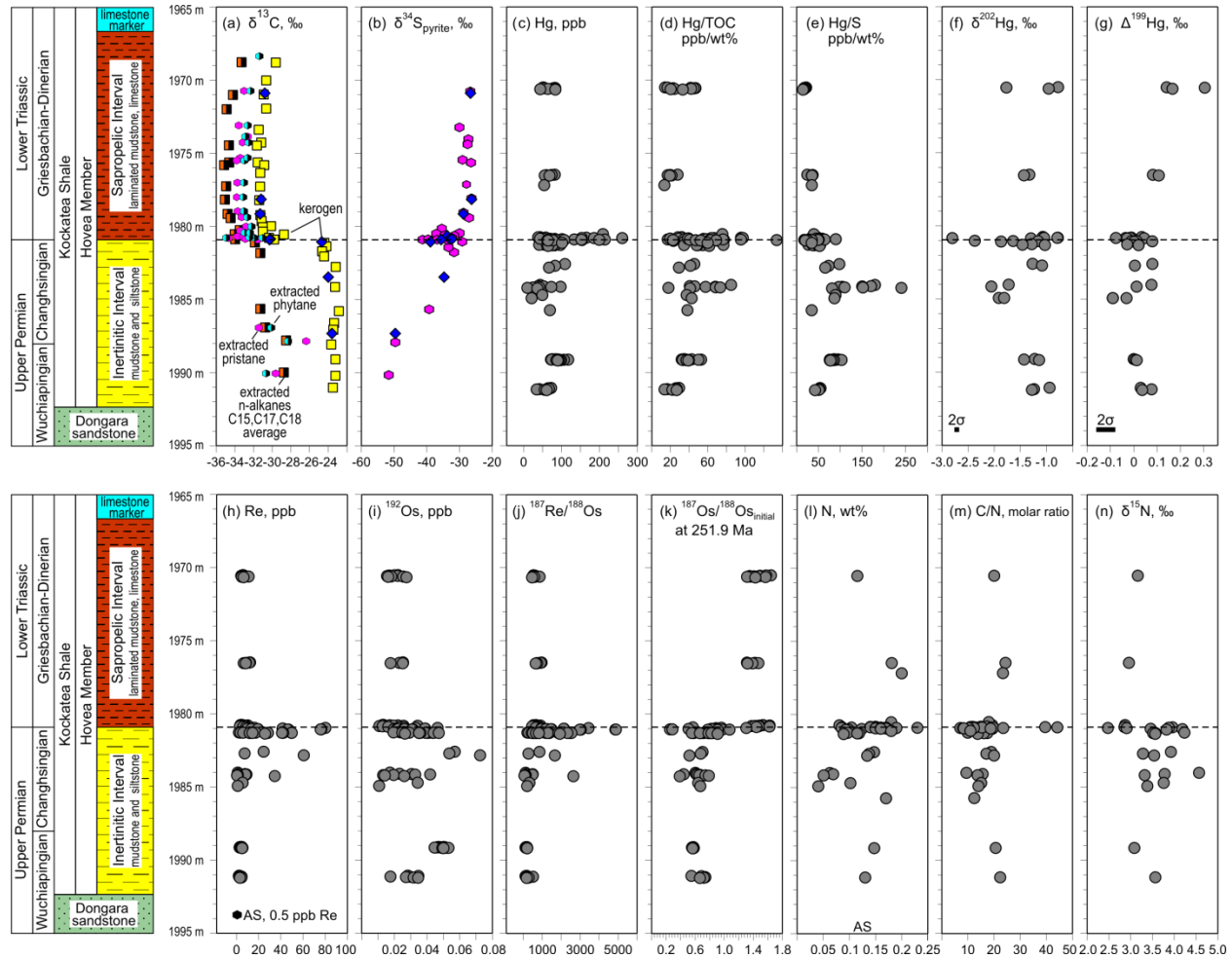
Figure 2. Stratigraphic variations of selected major and trace elements and their weight ratios, total organic carbon (TOC), carbonate content, Rock-Eval parameters, and $C_{33}n$-ACH/n-C_{34} biomarker ratio in the studied Hovea-3 section. Data from this study are plotted as gray circles and supplemented by published data re-drawn from Thomas et al., 2004 (TOC content, type and amount of OM, HI; squares), Gorter et al., 2009 (HI, T_{max}; diamonds), and from Grice et al., 2005b (biomarkers; hexes). Where available, we also show the typical elemental content and weight ratios in average shale (AS), plotted near the bottom of panels as black squares (values from Li et al., 1991) or black diamonds (values from Brumsack, 2006). Pyrite Fe/total Fe (panel g) is calculated assuming all sulfur in the sample is pyrite bound (see Georgiev et al., 2015 for discussion). This ratio provides a *minimum* estimates for both the highly reactive Fe/total Fe indicator for anoxic versus oxic bottom water (solid lines), and for the pyrite Fe/highly reactive Fe indicator for discrimination of euxinic versus ferruginous bottom water conditions for clearly

1125 anoxic samples (similar to degree of pyritization, dotted lines); boundaries from Poulton and

1126 Canfield (2011). Dashed horizontal line on each panel marks the boundary between the

1127 Inertinitic and Sapropelic Intervals.

1128

1129 **Figure 3.** Stratigraphic variations of selected elemental concentrations, weight ratios, and

1130 isotopic composition of Hovea-3 samples. Re-Os, Hg, and N elemental and isotopic data from

1131 this study are plotted as gray circles. Carbon, S, and H isotopic data are re-drawn from Thomas

1132 et al., 2004 (δ^{13}C of kerogen and solvent-extracted alkanes; squares) and from Grice et al., 2005a

1133 (δ^{13}C of extracted branched alkanes pristane and phytane, and δ^{34}S$_{pyrite}$; hexes), or taken from

1134 Nabbefeld et al., 2010a (δ^{13}C$_{kerogen}$, δ^{34}S$_{pyrite}$; diamonds). The initial Os ratios on panel (k) are

1135 calculated from measured Re-Os data using an input age of 251.9 Ma (P–Tr boundary).

1136 Alternative calculations using depositional ages from 259 Ma to 251.9 Ma for the different

1137 intervals result in similar Os-initial ratios with insignificant absolute changes (−0.09 to +0.01;

1138 average −0.02) compared with the observed Os-initial range between 0.25 and 1.64 (panel k);

1139   age-related uncertainties will be even smaller for the Triassic samples (Griasbachian age; low

1140   Re/Os ratios). A single sample from the lowermost studied interval yielded negative Os_i (not

1141   plotted). Dashed horizontal line on each panel marks the boundary between the Inertinitic and

1142   Sapropelic Intervals.
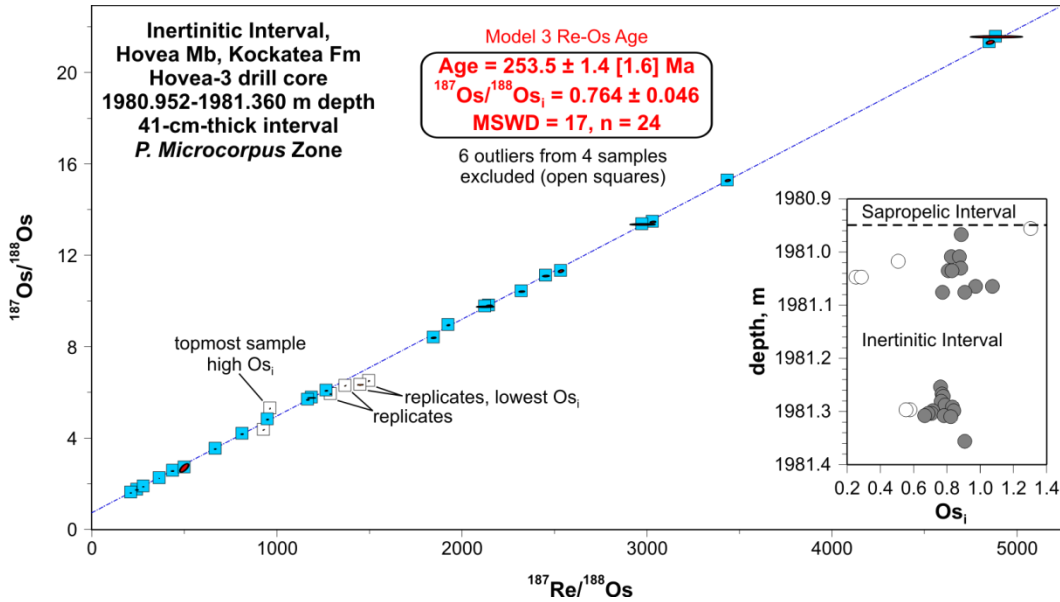
1143

1144   **Figure 4.** Re-Os isochron diagram for the uppermost Inertinitic Interval. Squares are added

1145   to highlight 2σ uncertainties (red ellipses). Age uncertainty reported in brackets includes the

1146 ^{187}Re decay constant uncertainty. The inset shows the Os_i for individual samples, calculated for

1147   251.9 Ma. Six outliers from four samples excluded from the isochron regression are plotted with
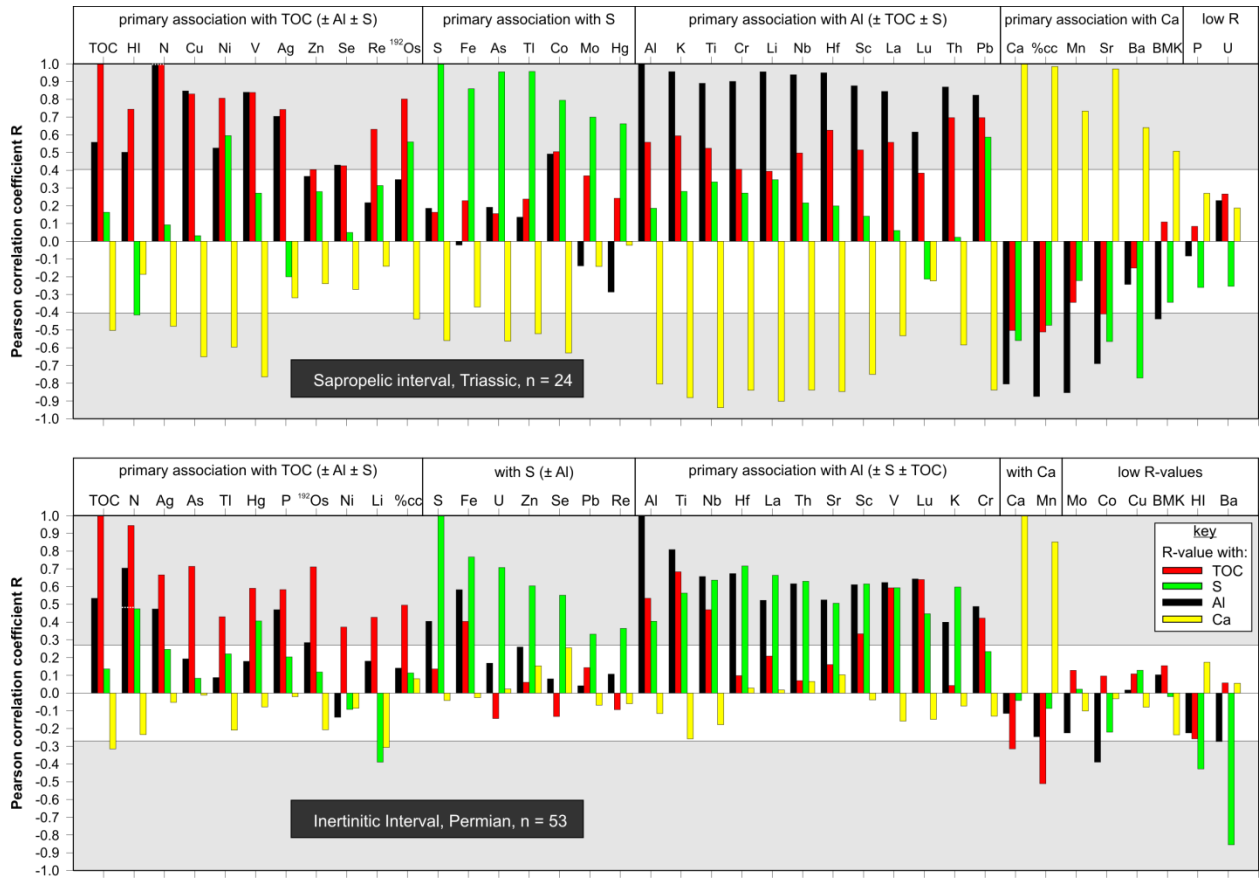
1148   open symbols.

Figure 5. Pearson correlation coefficients (R-values) of selected major and trace elements, carbonate contents (%cc), hydrogen indices (HI) and C_{33} *n*-ACH / *n*-C_{34} biomarker ratio (BMK) with TOC, S, Al, and Ca contents for the Sapropelic (top) and Inertinitic (bottom) Intervals. Shaded areas mark statistically significant correlations (p<0.05) valid for most data. Nitrogen data have different thresholds for statistical significance of r>0.997 for the Sapropelic Interval (n =3), and of r>0.483 for the Inertinitic Interval (n=17); these are marked by dotted white lines across the nitrogen data. Re-Os replicate analyses, and five samples from the boundary zone between the Sapropelic and Inertinitic Intervals that show mixed geochemical parameters were excluded from the calculations.
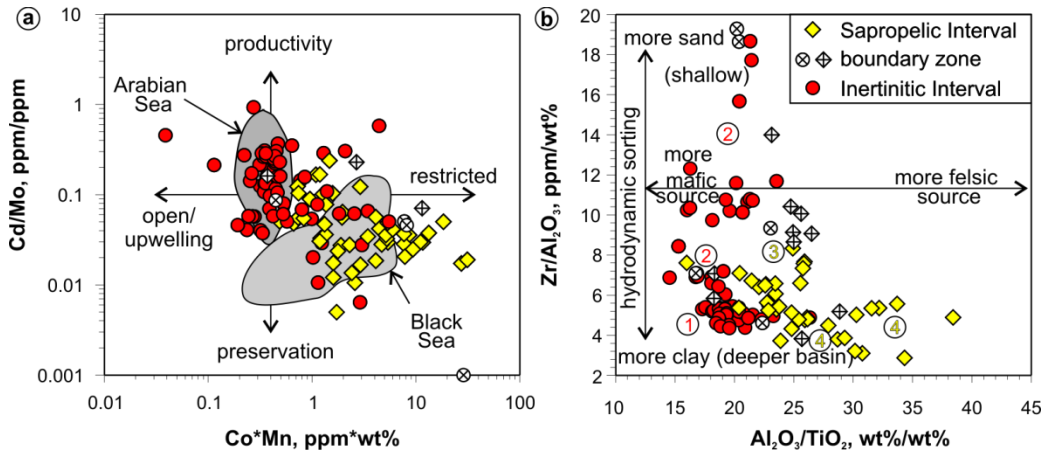
Figure 6. Trace metal constraints for the depositional setting of studied Hovea-3 shales. Panel (a) distinguishes between settings of basin restriction and of predominant upwelling, with additional constraints on the roles of productivity and preservation (plot and fields for modern-day Arabian and Black Seas from Sweere et al., 2016). A single point with Cd/Mo ratio of 0.0007 is plotted at the y-axis origin (Cd/Mo = 0.001). Panel (b) shows the geochemical effect of hydrodynamic sorting that can be related to water depths, and of changing provenance (after Garcia et al., 1994, and Greber and Dauphas, 2019). Circled numbers are used to trace general temporal trends of changing basin depth based mainly on the Zr/Al ratios in the following sample groups: 1) older Upper Permian samples at 1991, 1989, and 1984 m depth, 2) uppermost Permian samples at 1981 m depth; 3) lowermost Triassic samples at 1980 m depth; and 4) remaining Triassic samples at 1976 and 1970 m depth. Measured Al and Ti were converted to elemental oxides for ease of comparison with the literature data. See text for additional discussion.
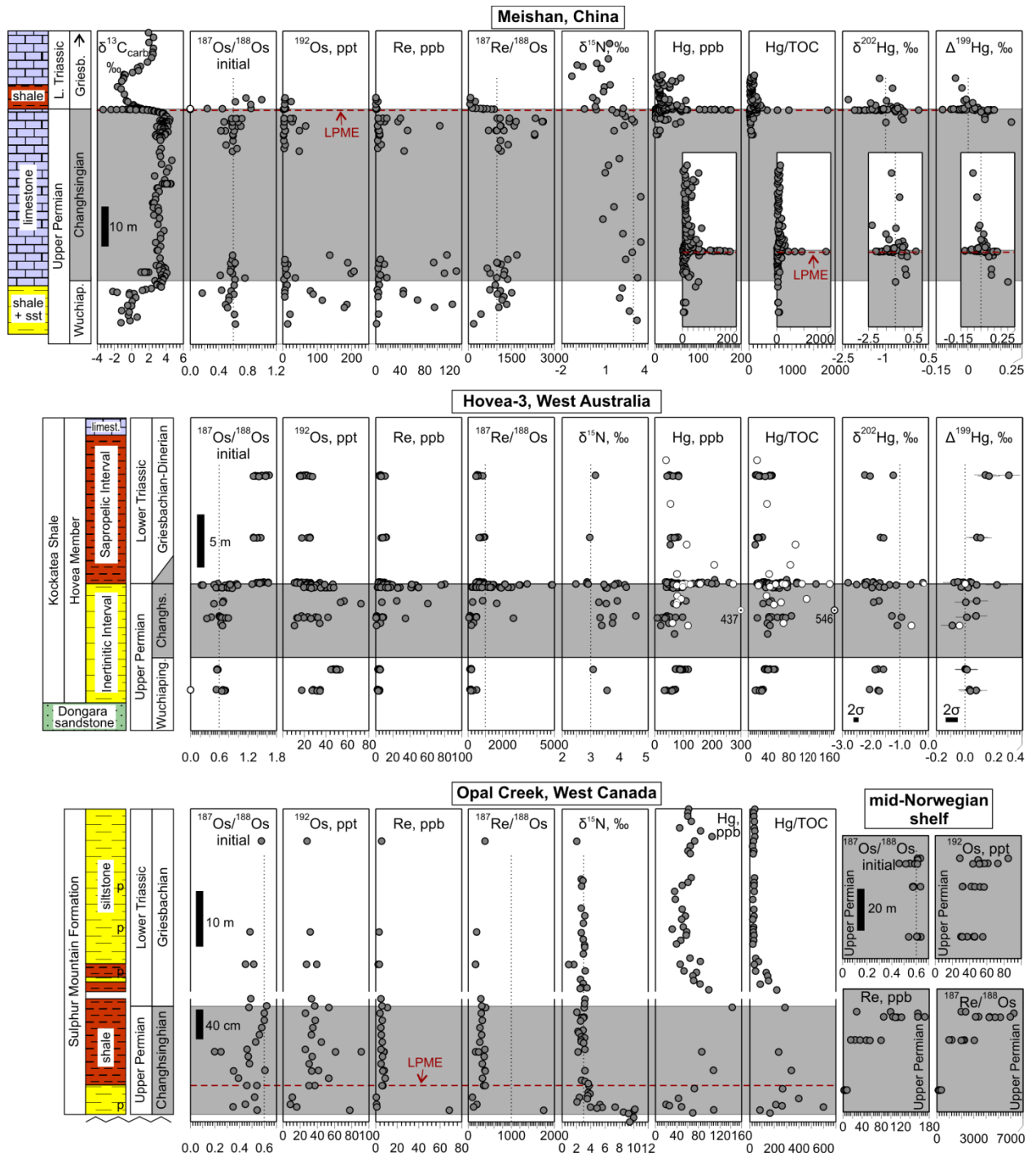
Figure 7. Stratigraphic variations in Re-Os, N, and Hg contents and isotopic composition across the Permian–Triassic boundary in Meishan, South China (top), Hovea-3 (middle), Opal Creek, West Canada (bottom), and in the Upper Permian mid-Norwegian shelf (bottom right) sections. Data for the Hovea-3 are from this study, with additional Hg data from a recent study by Sial et al. (2020) plotted as white circles for comparison (one of their samples shows

1179 anomalously high Hg contents and Hg/TOC ratios; values are indicated with numbers). Meishan

1180 section include general lithology and $\delta^{13}C_{carb}$ (Shen et al., 2013), Re-Os (Zhao et al., 2015; Liu et

1181 al., 2019), N (Cao et al., 2009), and Hg data (Shen et al., 2019). Data for the Opal Creek section

1182 include general lithology (letters "p" mark prominent pyrite layers) and Re-Os (Schoepfer et al.,

1183 2013; Georgiev et al., 2015a), N (Schoepfer et al., 2012; Georgiev et al., 2015a), and Hg data

1184 (Grasby et al., 2017; Wang et al., 2018; Shen et al., 2019). Re-Os data for Changhsingian (based

1185 on their Re-Os age) shales from the mid-Norwegian shelf are from Georgiev et al. (2011). The

1186 Changhsingian stage is highlighted in gray to facilitate visual comparison, with

1187 chronostratigraphic subdivision for the Hovea-3 section after Thomas et al. (2004); the upward

1188 revision for the P–Tr boundary proposed in Metcalfe et al. (2008) is shown as a gray triangle on

1189 the Hovea-3 chronostratigraphic column. Insets for Meishan Hg data show an expanded view on

1190 the P–Tr boundary interval. Note that the Opal Creek data are presented in two vertical scales to

1191 provide an expanded view of the lowermost 1.6 m of the section (Wuchiapingian to lowermost

1192 Triassic), where the most prominent geochemical changes occur. Dashed horizontal lines across

1193 the Meishan and Opal Creek panels mark the Late Permian mass extinction horizon (LPME). For

1194 ease of comparison between the sections, dotted vertical lines mark constant isotopic ratios as

1195 follows: initial $^{187}Os/^{188}Os = 0.6$, $^{187}Re/^{188}Os = 1000$, $\delta^{15}N = +3‰$, $\delta^{202}Hg = -1‰$, and $\Delta^{199}Hg =$

1196 $0‰$. Initial $^{187}Os/^{188}Os$ ratios are calculated at 252 Ma for the Opal Creek section, at 251.9, 253,

1197 and 256 Ma for the Triassic, Changhsingian and Wuchiapingian samples from Hovea-3,

1198 respectively, and at ages ranging from 251.8 to 253.9 Ma for the Meishan section (based on

1199 high-precision U-Pb ages); small differences in input ages up to few Ma have a generally

1200 insignificant effect on calculated Os initial ratios. Few samples from the Meishan section (bed

1201 27) and a single sample from the Hovea-3 section yield negative Os ratios that indicate Re-Os

1202 disturbance; these are plotted as white circles at $^{187}Os/^{188}Os = 0$.

1203

References:

1205 Algeo, T. J. and Lyons, T. W., 2006. Mo-total organic carbon covariation in modern anoxic

1206   marine environments: Implications for analysis of paleoredox and paleohydrographic

1207   conditions. Paleoceanography 21, p. 1016.

1208 Algeo, T. J. and Twitchett, R. J., 2010. Anomalous Early Triassic sediment fluxes due to

1209   elevated weathering rates and their biological consequences. Geology 38, 1023-1026.

1210   Archbold, N. W., 2000. Paleobiology of the Australasian Permian. Association of Australasian

1211   Palaeontologists Memoirs 23, 287-310.

1212   Bernasconi, S. M., Meier, I., Wohlwend, S., Brack, P., Hochuli, P. A., Bläsi, H., Wortmann, U.

1213   G., and Ramseyer, K., 2017. An evaporite-based high-resolution sulfur isotope record of Late

1214   Permian and Triassic seawater sulfate. Geochimica et Cosmochimica Acta 204, 331-349.

1215   Birck, J. L., RoyBarman, M., and Capmas, F., 1997. Re-Os isotopic measurements at the

1216   femtomole level in natural samples. Geostandards Newsletter 21, 19-27.

1217   Blum, J. D., Sherman, L. S., and Johnson, M. W., 2014. Mercury isotopes in earth and

1218   environmental sciences. Annual Review of Earth and Planetary Sciences 42, 249-269.

1219   Bottini, C., Cohen, A. S., Erba, E., Jenkyns, H. C., and Coe, A. L., 2012. Osmium-isotope

1220   evidence for volcanism, weathering, and ocean mixing during the early Aptian OAE 1a.

1221   Geology 40, 583-586.

1222   Böttcher, M. E., Hetzel, A., Brumsack, H. -J., and Schipper, A., 2006. Sulfur-iron-carbon

1223   geochemistry in sediments of the Demerara Rise. *In* Mosher, D. C., Erbacher, J., and Malone,

1224   M. J. (Eds.), *Proc. ODP, Sci. Results,* 207: College Station, TX (Ocean Drilling Program), 1–

1225   23.

1226   Bond, D. P. G. and Wignall, P. B., 2010. Pyrite framboid study of marine Permian–Triassic

1227   boundary sections: A complex anoxic event and its relationship to contemporaneous mass

1228   extinction. Geological Society of America Bulletin 122, 1265-1279.

1229   Bowring, S. A., Erwin, D. H., Jin, Y. G., Martin, M. W., Davidek, K. and Wang, W., 1998. U/Pb

1230   zircon geochronology and tempo of the end-Permian mass extinction. Science 280, 1039-

1231   1045.

1232   Brand, W. A. and Coplen, T. B., 2012. Stable isotope deltas: tiny, yet robust signatures in nature.

1233   Isotopes in Environmental and Health Studies 48, 393-409.

1234   Brumsack, H. J., 2006. The trace metal content of recent organic carbon-rich sediments:

1235   Implications for Cretaceous black shale formation. Palaeogeography Palaeoclimatology

1236   Palaeoecology 232, 344-361.

1237   Burgess, S. D., Bowring, S., and Shen, S. Z., 2014. High-precision timeline for Earth's most

1238   severe extinction. Proceedings of the National Academy of Sciences of the United States of

1239   America 111, 3316-3321.

Burgess, S., Muirhead, J., and Bowring, S., 2017. Initial pulse of Siberian Traps sills as the trigger of the end-Permian mass extinction. Nature Communications 8, 164.

Cao, C. Q., Love, G. D., Hays, L. E., Wang, W., Shen, S. Z., and Summons, R. E., 2009. Biogeochemical evidence for euxinic oceans and ecological disturbance presaging the end-Permian mass extinction event. Earth and Planetary Science Letters 281, 188-201.

Cohen, A. S. and Waters, F. G., 1996. Separation of osmium from geological materials by solvent extraction for analysis by thermal ionisation mass spectrometry. Analytica Chimica Acta 332, 269-275.

Cohen, A. S., Coe, A. L., Harding, S. M., and Schwark, L., 2004. Osmium isotope evidence for the regulation of atmospheric CO_2 by continental weathering. Geology 32, 157-160.

Cooper, G., Xiang, R., Agnew, N., Ward, P., Fabian, M., and Tupper, N., 2015. A systematic approach to unconventional play analysis: the oil and gas potential of the Kockatea Shale and Carynginia Formation, North Perth Basin, Western Australia. The APPEA Journal 55, 193-214.

Department of Water, 2017. Northern Perth Basin: Geology, hydrogeology and groundwater resources Hydrogeological bulletin series, report no. HB1, Department of Water, Government of Western Australia, Perth.

Erwin, D.H., 1994. The Permo-Triassic extinction. Nature 367, 231–236.

Estrade, N., Carignan, J., Sonke, J. E., and Donard, O. F., 2010. Measuring Hg isotopes in bio-geo-environmental reference materials. Geostandards and Geoanalytical Research 34, 79-93.

Foster, C., Logan, G., and Summons, R., 1998. The Permian–Triassic boundary in Australia: where is it and how is it expressed? Proceedings of the royal society of Victoria 110, 247-266.

Garcia, D., Fonteilles, M., and Moutte, J., 1994. Sedimentary fractionations between Al, Ti, and Zr and the genesis of strongly peraluminous granites. Journal of Geology 102, 411-422.

Georgiev, S., Stein, H. J., Hannah, J. L., Bingen, B., Weiss, H. M., and Piasecki, S., 2011. Hot acidic Late Permian seas stifle life in record time. Earth and Planetary Science Letters 310, 389-400.

Georgiev, S., Stein, H. J., Hannah, J. L., Weiss, H. M., Bingen, B., Xu, G., Rein, E., Hatlø, V., Løseth, H., Nali, M., and Piasecki, S., 2012. Chemical signals for oxidative weathering predict Re-Os isochroneity in black shales, East Greenland. Chemical Geology 324, 108-121.

Georgiev, S. V., Stein, H. J., Hannah, J. L., Henderson, C. M., and Algeo, T. J., 2015a. Enhanced recycling of organic matter and Os-isotopic evidence for multiple magmatic or meteoritic inputs to the Late Permian Panthalassic Ocean, Opal Creek, Canada. Geochimica et Cosmochimica Acta 150, 192-210.

Georgiev, S. V., Horner, T. J., Stein, H. J., Hannah, J. L., Bingen, B., and Rehkämper, M., 2015b. Cadmium-isotopic evidence for increasing primary productivity during the Late Permian anoxic event. Earth and Planetary Science Letters 410, 84-96.

Georgiev, S. V., Stein, H. J., Hannah, J. L., Xu, G. P., Bingen, B., and Weiss, H. M., 2017. Timing, duration, and causes for Late Jurassic-Early Cretaceous anoxia in the Barents Sea. Earth and Planetary Science Letters 461, 151-162.

Georgiev, S. V., Zimmerman, A., Yang, G., Goswami, V., Hurtig, N. C., Hannah, J. L., and Stein, H. J., 2018. Comparison of chemical procedures for Re-isotopic measurements by N-TIMS. Chemical Geology 483, 151-161.

Gorter, J., Nicoll, R. S., Metcalfe, I., Willink, R., and Ferdinando, D., 2009. The Permian–Triassic boundary in Western Australia: evidence from the Bonaparte and Northern Perth basins-exploration implications. The APPEA Journal 49, 311-336.

Gramlich, J. W., Murphy, T. J., Garner, E. L., and Shields, W. R., 1973. Absolute isotopic abundance ratio and atomic weight of a reference sample of rhenium. Journal of Research of the National Bureau of Standards - Physics and Chemistry A 77, 691-698.

Grasby, S. E., Shen, W. J., Yin, R. S., Gleason, J. D., Blum, J. D., Lepak, R. F., Hurley, J. P., and Beauchamp, B., 2017. Isotopic signatures of mercury contamination in latest Permian oceans. Geology 45, 55-58.

Greber, N. D. and Dauphas, N., 2019. The chemistry of fine-grained terrigenous sediments reveals a chemically evolved Paleoarchean emerged crust. Geochimica et Cosmochimica Acta 255, 247-264.

Grice, K., Cao, C. Q., Love, G. D., Böttcher, M. E., Twitchett, R. J., Grosjean, E., Summons, R. E., Turgeon, S. C., Dunning, W., and Jin, Y. G., 2005a. Photic zone euxinia during the Permian–Triassic superanoxic event. Science 307, 706-709.

Grice, K., Twitchett, R. J., Alexander, R., Foster, C. B., and Looy, C., 2005b. A potential biomarker for the Permian–Triassic ecological crisis. Earth and Planetary Science Letters 236, 315-321.

Grice, K., Summons, R., Grosjean, E., Twitchett, R., Dunning, W., Wang, S., and Böttcher, M.E., 2005c. Depositional conditions of the northern onshore Perth Basin (Basal Triassic). The APPEA Journal 45, 262-274.

Grice, K., Nabbefeld, B., and Maslen, E., 2007. Source and significance of selected polycyclic aromatic hydrocarbons in sediments (Hovea-3 well, Perth Basin, Western Australia) spanning the Permian–Triassic boundary. Organic Geochemistry 38, 1795-1803.

Grotheer, H., Le Métayer, P., Piggott, M., Lindeboom, E., Holman, A., Twitchett, R., and Grice, K., 2017. Occurrence and significance of phytanyl arenes across the Permian–Triassic boundary interval. Organic Geochemistry 104, 42-52.

Hartmann, M. and Nielsen, H., 2012. $\delta^{34}S$ values in recent sea sediments and their significance using several sediment profiles from the western Baltic Sea. Isotopes in Environmental and Health Studies 48, 7-32.

Hetzel, A., Böttcher, M. E., Wortmann, U. G., and Brumsack, H. -J., 2009. Paleo-redox conditions during OAE 2 reflected in Demerara Rise sediment geochemistry (ODP Leg 207) Palaeogeography, Palaeoclimatology, Palaeoecology 273, 302-328.

Holman, A. I., Greenwood, P. F., Brocks, J. J., and Grice, K., 2014. Effects of sulfide minerals on aromatic maturity parameters: Laboratory investigation using micro-scale sealed vessel pyrolysis. Organic Geochemistry 76, 270-277.

Jin, Y. G., Wang, Y., Wang, W., Shang, Q. H., Cao, C. Q., and Erwin, D. H., 2000. Pattern of marine mass extinction near the Permian–Triassic boundary in South China. Science 289, 432-436.

Jones, M. T., Percival, L. M. E., Stokke, E. W., Frieling, J., Mather, T. A., Riber, L., Schubert, B. A., Schultz, B., Tegner, C., Planke, S., and Svensen, H. H., 2019. Mercury anomalies across the Palaeocene-Eocene Thermal Maximum. Clim. Past 15, 217-236.

Jørgensen, B. B., Böttcher, M. E., Lüschen, H., Neretin, L. N. and Volkov, I. I., 2004. Anaerobic methane oxidation and a deep H_2S sink generate isotopically heavy sulfides in Black Sea sediments. Geochimica et Cosmochimica Acta 68, 2095-2118.

Knoll, A.H., Bambach, R.K., Payne, J.L., Pruss, S. and Fischer, W.W., 2007. Paleophysiology and end-Permian mass extinction. Earth and Planetary Science Letters 256, 3-4, 295-313.

Kowalski, N., Dellwig, O., Beck, M., Grunwald, M., Badewien, T., Brumsack, H. -J., van Beusekom, J. E. E., and Böttcher, M. E., 2012. A comparative study of manganese dynamics

in pelagic and benthic parts of two tidal systems of the North Sea. Estuarine and Coastal Shelf Sciences 100, 3-17.

Leipe, T., Moros, M., Kotilainen, A.T., Vallius, H., Kabel, K., Endler, M., Kowalski, N., 2013. Mercury in Baltic Sea sediments—Natural background and anthropogenic impact. Chemie der Erde - Geochemistry 73, 249–259.

Li, Y. H., 1991. Distribution patterns of the elements in the ocean - a synthesis. Geochimica et Cosmochimica Acta 55, 3223-3240.

Liu, Z., Selby, D., Zhang, H., Zheng, Q., Shen, S., Sageman, B. B., Grasby, S. E., and Beauchamp, B., 2019. Osmium-isotope evidence for volcanism across the Wuchiapingian-Changhsingian boundary interval. Chemical Geology 529, 119313.

Ludwig, K.R., 2003. User's manual for Isoplot 3.00. A geochronological toolkit for Microsoft Excel. In: Berkeley Geochronology Center Special Publication, vol. 4, 71 pp.

Marie, B., Marin, L., Martin, P. Y., Gulon, T., Carignan, J., and Cloquet, C., 2015. Determination of mercury in one hundred and sixteen geological and environmental reference materials using a direct mercury analyser. Geostandards and Geoanalytical Research 39, 71-86.

McArthur, J. M., Algeo, T. J., van de Schootbrugge, B., Li, Q., and Howarth, R. J., 2008. Basinal restriction, black shales, Re-Os dating, and the Early Toarcian (Jurassic) oceanic anoxic event. Paleoceanography 23, PA4217, 1-22.

Meier, M. M., Cloquet, C., and Marty, B., 2016. Mercury (Hg) in meteorites: Variations in abundance, thermal release profile, mass-dependent and mass-independent isotopic fractionation. Geochimica et Cosmochimica Acta 182, 55-72.

Metcalfe, I., Nicoll, R. S., and Willink, R. J., 2008. Conodonts from the Permian - Triassic transition in Australia and position of the Permian - Triassic boundary. Australian Journal of Earth Sciences 55, 365-377.

Metcalfe, I., Crowley, J. L., Nicoll, R. S., and Schmitz, M., 2015. High-precision U-Pb CA-TIMS calibration of Middle Permian to Lower Triassic sequences, mass extinction and extreme climate-change in eastern Australian Gondwana. Gondwana Research 28, 61-81.

Morse, J. W. and Luther III, G. W., 1999. Chemical influences on trace metal-sulfide interactions in anoxic sediments. Geochimica et Cosmochimica Acta, 63, 3373-3378.

1362 Nabbefeld, B., Grice, K., Schimmelmann, A., Sauer, P. E., Böttcher, M. E., and Twitchett, R.,
1363   2010a. Significance of $\delta D_{kerogen}$, $\delta^{13}C_{kerogen}$ and $\delta^{34}S_{pyrite}$ from several Permian/Triassic (P/Tr)
1364   sections. Earth and Planetary Science Letters 295, 21-29.

1365 Nabbefeld, B., Grice, K., Schimmelmann, A., Summons, R. E., Troitzsch, U., and Twitchett, R.
1366   J., 2010b. A comparison of thermal maturity parameters between freely extracted
1367   hydrocarbons (Bitumen I) and a second extract (Bitumen II) from within the kerogen matrix
1368   of Permian and Triassic sedimentary rocks. Organic Geochemistry 41, 78-87.

1369 Neretin, L. N., Böttcher, M. E., and Grinenko, V. A., 2003. Sulfur isotope geochemistry of the
1370   Black Sea water column. Chemical Geology 200, 59-69.

1371 Nier, A. O., 1950. A redetermination of the relative abundances of the isotopes of carbon,
1372   nitrogen, oxygen, argon, and potassium. Physical Review 77, 789-793

1373 Payne, J. L. and Clapham, M. E., 2012. End-Permian mass extinction in the oceans: an ancient
1374   analog for the twenty-first century? Annual Review of Earth and Planetary Sciences 40, 89-
1375   111

1376 Peters, K. E., 1986. Guidelines for evaluating petroleum source rock using programmed
1377   pyrolysis. AAPG Bulletin 70, 318-329.

1378 Peucker-Ehrenbrink, B. and Ravizza, G., 2000. The marine osmium isotope record. Terra Nova
1379   12, 205-219.

1380 Poulton, S. W. and Canfield, D. E., 2011. Ferruginous conditions: A dominant feature of the
1381   ocean through Earth's history. Elements 7, 107-112.

1382 Quan, T. M., Wright, J. D., and Falkowski, P. G., 2013. Co-variation of nitrogen isotopes and
1383   redox states through glacial–interglacial cycles in the Black Sea. Geochimica et
1384   Cosmochimica Acta 112, 305-320.

1385 Rampino, M. R. and Caldeira, K., 2005. Major perturbation of ocean chemistry and a
1386   'Strangelove Ocean' after the end-Permian mass extinction. Terra Nova 17, 554-559.

1387 Rimmer, S. M., 2004. Geochemical paleoredox indicators in Devonian-Mississippian black
1388   shales, central Appalachian basin (USA). Chemical Geology 206, 373-391.

1389 Schoepfer, S. D., Henderson, C. M., Garrison, G. H., and Ward, P. D., 2012. Cessation of a
1390   productive coastal upwelling system in the Panthalassic Ocean at the Permian–Triassic
1391   Boundary. Palaeogeography Palaeoclimatology Palaeoecology 313, 181-188.

1392 Schoepfer, S. D., Henderson, C. M., Garrison, G. H., Foriel, J., Ward, P. D., Selby, D., Hower, J.
1393   C., Algeo, T. J., and Shen, Y., 2013. Termination of a continent-margin upwelling system at
1394   the Permian–Triassic boundary (Opal Creek, Alberta, Canada). Global and Planetary Change
1395   105, 21-35.

1396 Scaife, J. D., Ruhl, M., Dickson, A. J., Mather, T. A., Jenkyns, H. C., Percival, L. M. E.,
1397   Hesselbo, S. P., Cartwright, J., Eldrett, J. S., Bergman, S. C., Minisini, D., 2017. Sedimentary
1398   mercury enrichments as a marker for submarine Large Igneous Province volcanism?
1399   Evidence from the Mid-Cenomanian Event and Oceanic Anoxic Event 2 (Late Cretaceous).
1400   Geochemistry Geophysics Geosystems · November 2017 DOI:
1401   10.1002/2017gc007153

1402 Scotese, C. R., 2014. Map Folio 49, Permo-Triassic Boundary (251 Ma). Atlas of Middle & late
1403   Permian and Triassic paleogeographic maps, maps 43–48 from volume 3 of the PALEOMAP
1404   atlas for ArcGIS (Jurassic and Triassic) and maps 49–52 from volume 4 of the PALEOMAP
1405   PaleoAtlas for ArcGIS (late Paleozoic), mollweide projection. Evanston, IL: PALEOMAP
1406   Project.

1407 Sepkoski Jr., J. J., 2002. A compendium of fossil marine animal genera. Bull. Am. Paleontol.
1408   363, 1–563.Shen, W. J., Sun, Y. G., Lin, Y. T., Liu, D. H., and Chai, P. X., 2011. Evidence
1409   for wildfire in the Meishan section and implications for Permian–Triassic events.
1410   Geochimica et Cosmochimica Acta 75, 1992-2006.

1411 Shen, S. Z., Cao, C. Q., Zhang, H., Bowring, S. A., Henderson, C. M., Payne, J. L., Davydov, V.
1412   I., Chen, B., Yuan, D. X., Zhang, Y. C., Wang, W., and Zheng, Q. F., 2013. High-resolution
1413 $\delta^{13}C_{carb}$ chemostratigraphy from latest Guadalupian through earliest Triassic in South China
1414   and Iran. Earth and Planetary Science Letters 375, 156-165.

1415 Shen, J., Chen, J. B., Algeo, T. J., Yuan, S. L., Feng, Q. L., Yu, J. X., Zhou, L., O'Connell, B.,
1416   and Planavsky, N. J., 2019a. Evidence for a prolonged Permian–Triassic extinction interval
1417   from global marine mercury records. Nature Communications 10.

1418 Shen, J., Yu, J., Chen, J., Algeo, T. J., Xu, G., Feng, Q., Shi, X., Planavsky, N. J., Shu, W., and
1419   Xie, S., 2019b. Mercury evidence of intense volcanic effects on land during the Permian–
1420   Triassic transition. Geology, 47, 1117-1121.

Shen, J., Algeo, T. J., Chen, J., Planavsky, N. J., Feng, Q., Yu, J., Liu, J., 2019c. Mercury in marine Ordovician/Silurian boundary sections of South China is sulfide-hosted and non-volcanic in origin. Earth and Planetary Science Letters 511, 130-140.

Sial, A., Chen, J., Lacerda, L., Korte, C., Spangenberg, J., Silva-Tamayo, J., Gaucher, C., Ferreira, V., Barbosa, J., and Pereira, N., 2020. Globally enhanced Hg deposition and Hg isotopes in sections straddling the Permian–Triassic boundary: Link to volcanism. Palaeogeography, Palaeoclimatology, Palaeoecology 540, 109537.

Stein, H.J., 2014. Dating and Tracing the History of Ore Formation, *in* Holland, H.D. and Turekian, K.K. (editors) Treatise on Geochemistry, Second Edition, v. 13, p. 87-118. Oxford: Elsevier.

Sun, Y. D., Joachimski, M. M., Wignall, P. B., Yan, C. B., Chen, Y. L., Jiang, H. S., Wang, L. N., and Lai, X. L., 2012. Lethally hot temperatures during the Early Triassic greenhouse. Science 338, 366-370.

Sun, Y., Zulla, M., Joachimski, M., Bond, D., Wignall, P., Zhang, Z., and Zhang, M., 2019. Ammonium ocean following the end-Permian mass extinction. Earth and Planetary Science Letters 518, 211-222.

Svensen, H., Planke, S., Polozov, A. G., Schmidbauer, N., Corfu, F., Podladchikov, Y. Y., and Jamtveit, B., 2009. Siberian gas venting and the end-Permian environmental crisis. Earth and Planetary Science Letters 277, 490-500.

Them, T. R., Jagoe, C. H., Caruthers, A. H., Gill, B. C., Grasby, S. E., Gröcke, D. R., Yin, R., and Owens, J. D., 2019. Terrestrial sources as the primary delivery mechanism of mercury to the oceans across the Toarcian Oceanic Anoxic Event (Early Jurassic). Earth and Planetary Science Letters 507, 62-72.

Thomas, B. and Barber, C., 2004. A re-evaluation of the hydrocarbon habitat of the northern Perth Basin. The APPEA Journal 44, 59-92.

Thomas, B. M., Willink, R. J., Grice, K., Twitchett, R. J., Purcell, R. R., Archbold, N. W., George, A. D., Tye, S., Alexander, R., Foster, C. B., and Barber, C. J., 2004. Unique marine Permian–Triassic boundary section from Western Australia. Australian Journal of Earth Sciences 51, 423-430.

1450   Turgeon, S. C., and Brumsack, H. -J., 2006. Anoxic vs dysoxic events reflected in sediment

1451   geochemistry during the Cenomanian-Turonian boundary event (Cretaceous) in the Umbria-Marche

1452   basin of central Italy. Chemical Geology 234, 321 – 339.

1453   Turgeon, S. C. and Creaser, R. A., 2008. Cretaceous oceanic anoxic event 2 triggered by a

1454   massive magmatic episode. Nature 454, 323-326.

1455   Tribovillard, N., Algeo, T. J., Lyons, T., and Riboulleau, A., 2006. Trace metals as paleoredox

1456   and paleoproductivity proxies: an update. Chemical Geology 232, 12-32.

1457   Volk, H., George, S., Boreham, C., and Kempton, R., 2004. Geochemical and compound specific

1458   carbon isotopic characterisation of fluid inclusion oils from the offshore Perth Basin,

1459   Western Australia: implications for recognising effective oil source rocks. The APPEA

1460   Journal 44, 223-240.

1461   Wang, X., Cawood, P. A., Zhao, H., Zhao, L., Grasby, S. E., Chen, Z.-Q., Wignall, P. B., Lv, Z.,

1462   and Han, C., 2018. Mercury anomalies across the end Permian mass extinction in South

1463   China from shallow and deep water depositional environments. Earth and Planetary Science

1464   Letters 496, 159-167.

1465   Wang, X. D., Cawood, P. A., Zhao, H., Zhao, L. S., Grasby, S. E., Chen, Z. Q., and Zhang, L.,

1466   2019. Global mercury cycle during the end-Permian mass extinction and subsequent Early

1467   Triassic recovery. Earth and Planetary Science Letters 513, 144-155.

1468   Wedepohl, K.H., 1991. The composition of the upper earth's crust and the natural cycles of

1469   selected metals. Metals in natural raw materials. Natural Resources. In: Merian, E. (Ed.),

1470   Metals and Their Compounds in the Environment.VCH, Weinheim, pp. 3 – 17.

1471   Wegwerth, A., Kaiser, J., Dellwig, O., Shumilovskikh, O. S., Nowaczyk, N. R., and Art, H.,

1472   2016. Northern hemisphere climate control on the environmental dynamics in the glacial

1473   Black Sea Lake. Quaternary Science Reviews 135, 41-53.

1474   Wilkin, R. T., Barnes, H. L., and Brantley, S. L., 1996. The size distribution of framboidal pyrite

1475   in modern sediments: An indicator of redox conditions. Geochimica et Cosmochimica Acta

1476   60, 3897-3912.

1477   Xu, G., Hannah, J. L., Bingen, B., Georgiev, S., and Stein, H. J., 2012. Digestion methods for

1478   trace element measurements in shales: paleoredox proxies examined. Chemical Geology 324,

1479   132-147.

1480 Yamashita, Y., Takahashi, Y., Haba, H., Enomoto, S., and Shimizu, H., 2007. Comparison of

1481 reductive accumulation of Re and Os in seawater - sediment systems. Geochimica et

1482 Cosmochimica Acta 71, 3458-3475.

1483 Zhao, H., Li, C., Jiang, X., Zhou, L., Li, X., Qu, W., and Du, A., 2015. Direct radiometric dating

1484 of limestone from Changxing Permian–Triassic boundary using the Re-Os geochronometer.

1485 Chinese Science Bulletin 60, 2209-2215 (in Chinese, with English abstract).

1486 Zheng, W., Gilleaudeaua, G. J., Kah, L. C., and Anbar, A. D., 2018. Mercury isotope signatures

1487 record photic zone euxinia in the Mesoproterozoic Ocean. Proceedings of the National

1488 Academy of Sciences of the United States of America 115, 10594-10599.